

Université de Montréal

Identification of urban surface materials using high-resolution hyperspectral aerial imagery

Par

Meghana Paranjape

Département de Géographie

Faculté des Arts et des Sciences

Mémoire présenté en vue de l'obtention du grade de Maître ès sciences (M.Sc.) en géographie

Juillet 2019

© Paranjape, 2019

Université de Montréal
Département de Géographie, Faculté des Arts et des Sciences

Ce mémoire intitulé:

**Identification of urban surface materials using high-resolution hyperspectral aerial
imagery**

(Identification des matériaux de surface urbaine par imageries aériennes hyperspectrales à haute
résolution)

Présenté par :
Meghana Paranjape

A été évalué par un jury composé des personnes suivantes

Liliana Perez
Président-rapporteur

François Cavayas
Directeur de recherche

Margaret Kalacska
Membre du jury

Abstract

Knowledge of surface cover materials is crucial for urban planning and management. With advances in remote sensing, especially in high spatial and spectral resolution imagery, the identification and detailed mapping of surface materials in urban areas based on spectral signatures are now feasible. Spectral signatures describe the interactions between ground objects and solar radiation and are assumed unique for each type of material.

In this research, we use airborne CASI images with 1 m² spatial resolution, with 96 contiguous bands in a spectral range between 367 nm and 1044 nm. These images covering the island of Montreal (Quebec, Canada), obtained in 2016, were analyzed to identify urban surface materials. The objectives of the project were first to find a correspondence between the physical and chemical characteristic of typical surface materials, present in the Montreal scenes, and the spectral signatures within the images. Second, to develop a sound methodology for identifying these surface materials in urban landscapes.

To reach these objectives, our method of analysis is based on a comparison of pixel spectral signatures to those contained in a reference spectral library that describe typical surface covering materials (inert materials and vegetation). Two metrics were used in order to measure the correspondence of pixel spectral signatures and reference spectral signature. The first metric considers the shape of a spectral signature and the second the difference of reflectance values between the observed and reference spectral signature. A fuzzy classifier using these two metrics is then applied to recognize the type of material on a pixel basis. Typical spectral signatures were extracted from two spectral libraries (ASTER and HYPERCUBE). Spectral signatures of typical objects in Montreal measured on the ground (ASD spectroradiometer) were also used as reference spectra. Three general types of surface materials (asphalt, concrete, and vegetation) were used to ease the comparison between classifications using these spectral libraries. The classification using ASTER as a reference library had the highest success rate reaching 92%, followed by the field spectra at 88%, and finally with HYPERCUBE at 80%. There were no significant differences in the classification results indicating that the methodology works independently of the source of reference spectral signatures.

Keywords: Hyperspectral Remote Sensing – Fuzzy Classification – Urban Surface Materials

Résumé

La connaissance des matériaux de surface est essentielle pour l'aménagement et la gestion des villes. Avec les avancées en télédétection, particulièrement en imagerie de haute résolution spatiale et spectrale, l'identification et la cartographie détaillée des matériaux de surface en milieu urbain sont maintenant envisageables. Les signatures spectrales décrivent les interactions entre les objets au sol et le rayonnement solaire, et elles sont supposées uniques pour chaque type de matériau de surface.

Dans ce projet de recherche nous avons utilisé des images hyperspectrales aériennes du capteur CASI, avec une résolution de 1 m² et 96 bandes contigües entre 380nm et 1040nm. Ces images couvrant l'île de Montréal (QC, Canada), acquises en 2016, ont été analysées pour identifier les matériaux de surfaces.

Pour atteindre ces objectifs, notre méthode d'analyse est fondée sur la comparaison des signatures spectrales d'un pixel quelconque à celles des objets typiques contenues dans des bibliothèques spectrales (matériaux inertes et végétation). Pour mesurer la correspondance entre la signature spectrale d'un objet et la signature spectrale de référence nous avons utilisé deux métriques. La première métrique tient compte de la forme d'une signature spectrale et la seconde, de la différence des valeurs de réflectance entre la signature spectrale observée et celle de référence. Un classificateur flou utilisant ces deux métriques est alors appliqué afin de reconnaître le type de matériau de surface sur la base du pixel. Des signatures spectrales typiques ont été extraites des deux bibliothèques spectrales (ASTER et HYPERCUBE). Des signatures spectrales des objets typiques à Montréal mesurées sur le terrain (spectroradiomètre ASD) ont été aussi utilisées comme références.

Trois grandes catégories de matériaux ont été identifiées dans les images pour faciliter la comparaison entre les classifications par source de références spectrales : l'asphalte, le béton et la végétation. La classification utilisant ASTER comme bibliothèque de référence a eu le plus grand taux de réussite avec 92%, suivi par ASD à 88% et finalement HYPERCUBE avec 80%. Nous

n'avons pas trouvé de différences significatives entre les trois résultats, ce qui indique que la classification est indépendante de la source des signatures spectrales de référence.

Mots-clés : Imagerie hyperspectrale – Classification floue – Matériaux de surface urbaine

Table of contents

ABSTRACT	3
RÉSUMÉ	4
TABLE OF CONTENTS	6
LIST OF TABLES	8
LIST OF FIGURES	9
LIST OF ABBREVIATIONS	11
ACKNOWLEDGEMENT	12
CHAPTER 1 - INTRODUCTION	13
1. CONTEXT AND PROBLEM STATEMENT	13
<i>1.1. Urban planning and management</i>	13
<i>1.1. Problem statement</i>	14
1.2. STUDY OBJECTIVES AND HYPOTHESES:	14
1.3. THESIS STRUCTURE	15
CHAPTER 2 - URBAN REMOTE SENSING WITH HYPERSPECTRAL IMAGES:	
BACKGROUND	16
2.1. SENSORS TYPES AND RESOLUTIONS FOR URBAN REMOTE SENSING	16
2.2. HYPERSPECTRAL IMAGERY: PROCESSING AND ANALYSIS.....	20
<i>2.2.1 Extraction of spectral signatures</i>	22
<i>2.2.2 Identification of surface cover materials</i>	24
2.3 PARTIAL CONCLUSIONS	31
CHAPTER 3 - PRELIMINARY STUDIES	32
3.1. CASI IMAGERY ANALYSIS	33
<i>3.1.1. Methodology of preliminary study with CASI 1500 imagery</i>	37
<i>3.1.2. Spectral unmixing</i>	38
<i>3.1.3. Results and discussion</i>	43
<i>3.1.4. Conclusion</i>	45

3.2. MULTISPECTRAL IMAGERY RGBI	47
3.2.1. <i>K-means algorithm</i>	47
3.2.2. <i>Results and validation</i>	48
3.2.3. <i>Conclusion RGBI images</i>	51
3.3. CONCLUSIONS ON PRELIMINARY RESULTS	51
CHAPTER 4 – METHODOLOGY	53
4.1. STUDY AREA	53
4.2. METHODOLOGY	57
4.2.1. <i>Preprocessing: Atmospheric Corrections</i>	57
4.2.2. <i>Image analysis: A combined classification methodology</i>	61
CHAPTER 5 – RESULTS AND DISCUSSION.....	75
5.1. RESULTS.....	77
5.1.1. <i>Confusion matrix for ASTER</i>	77
5.1.2. <i>Confusion matrix for HYPERCUBE</i>	78
5.1.3. <i>Confusion matrix for ASD</i>	79
5.1.4. <i>Comparison of confusions matrices</i>	80
5.2. DISCUSSION.....	81
5.2.1. <i>Discrepancies in results</i>	81
5.2.2. <i>Methodological errors:</i>	87
5.2.3. <i>Significant differences</i>	88
CHAPTER 6 – CONCLUSION AND FUTURE RESEARCH	89
BIBLIOGRAPHY	91

List of Tables

Table 2 Kappa coefficient and Variance of kappa coefficient of K-means classification with RGBI images.....	50
Table 3 Significance test using Z-score between K-means classification of RGBI images with points under shadows and without points under shadows (NS- not significant)	51
Table 4 Confusion matrix using ASTER library as reference spectra with N=50 comparing three classes, Asphalt, Concrete, and Vegetation	77
Table 5 Producer and user accuracy, omission and commission error of classification with ASTER library	77
Table 6 Confusion matrix using HYPERCUBE library with N=50 comparing three classes: Asphalt, Concrete, and Vegetation	78
Table 7 Producer and user accuracy, and omission and commission error for the classification using HYPERCUBE library	78
Table 8 Confusion matrix using ASD library with N=50 comparing three classes: Asphalt, Concrete, and Vegetation.....	79
Table 9 Producer and user accuracy, and omission and commission error of classification using ASD library.....	80
Table 10 Pairwise z-score to assess the significant difference between classification based on reference spectral signatures	80
Table 11 Spectral signatures remaining after classification of each reference spectral library	82

List of Figures

Figure 1 Graphical representation of sensors and their uses based on spatial, spectral, temporal, and radiometric resolution (source: Kadhim, Mourshed, and Bray 2016)	17
Figure 2 Comparison of spatial resolution between two images of the same urban scene : A. an aerial imagery with 1m spatial resolution, and B. an aerial imagery with 25cm spatial resolution.....	18
Figure 3 The electromagnetic spectrum.....	20
Figure 4 Diagram of radiance (adpated from Bonn and Guy 1993).....	20
Figure 5 Hyperspectral data cube (source: Shaw and Manolakis 2002).....	21
Figure 6 Apparent spectral signature in radiance units multiplied by a factor of 1000 of pixel covered by vegetation extracted from an airborne CASI1500 image (1m spatial resolution) with 96 bands between 350 nm and 1100 nm.....	22
Figure 7 Schema of a mixed pixels and the linear combination of the spectral signatures it is composed of vegetation, background soil, minerals, and manmade materials (Source: Geo University, website: https://www.geo.university/courses/the-network-based-method-spectral-unmixing-framework).....	29
Figure 8 Interactions of photons causing a non-linearly mixed pixel (source: Dobigeon et al. 2014)	30
Figure 9 Study area with flight lines of CASI 1500 hyperspectral aerial imagery.....	34
Figure 10 The borough of Montreal North: mosaic of CASI 1500 hyperspectral imagery (true color composite bands 14 in blue, 28 in green, and 42 in red)) with the flight lines covering it	36
Figure 11 Flowchart of preliminary analysis to identify urban surface materials using linear spectral unmixing.....	37
Figure 12 Spectral signatures of asphalt and concrete (between 440nm and 2400nm) (source: Herold et al. 2004)).....	39
Figure 13 Linear spectral unmixing results using hyperspectral CASI 1500 imagery of Montreal North (Montreal, Qc, Canada), bright shades represent higher proportions of vegetation, while dark shades represent lower portions of vegetation.....	40
Figure 14 Linear spectral unmixing results using hyperspectral CASI 1500 imagery of Montreal North (Montreal, Qc, Canada), bright shades represent higher proportions of asphalt, while dark shades represent lower portions of asphalt	41
Figure 15 Linear spectral unmixing results using hyperspectral CASI 1500 imagery of Montreal North (Montreal, Qc, Canada), bright shades represent higher proportions of concrete, while dark shades represent lower portions of concrete.....	42
Figure 16 Modal filter.....	43
Figure 17 Miss-positioning of validation points: two points said to be 'ready to plant' falling on an asphalt road	44
Figure 18 Concrete represented as bright pixels after linear spectral unmixing showing the potential for identifying urban surface materials.....	46
Figure 19 Differences in illuminations of two CASI images of the same scene taken on two separate days with different atmospheric conditions	46

Figure 20 Urban surface materials at potential planting points of a portion of Montreal North, Montreal, (QC) Canada.....	47
Figure 21 Urban surface materials of a portion of Montreal North using K-means clustering with RGBI 20cm ortho-images.....	49
Figure 22 Flowchart of the fuzzy classification methodology used to identify urban surface materials with hyperspectral data.....	53
Figure 23 Map of Montreal, Qc, Canada, showing the main land uses (source: Communauté Métropolitaine de Montréal (CMM), website: http://cmm.qc.ca/donnees-et-territoire/observatoire-grand-montreal/produits-cartographiques/cartes-pdf/).....	55
Figure 24 Study area for fuzzy classification tile CASI_2016_08_20_103450h14v1	56
Figure 25 Schema of flight line and field of view angle in the particular case of CASI 1500 hyperspectral imagery taken over the Island of Montreal (QC), Canada	60
Figure 26 Field of view from aerial imagery with CASI 1500 sensor in a Northward direction and a Southward direction	61
Figure 27 List of spectral signatures from ASTER library used as reference spectra.....	63
Figure 28 Graphical representation of spectral signatures in the ASTER library (conifers in green, construction concrete in blue, and black tar in black).....	63
Figure 29 List of the spectral signatures from HYPERCUBE library used as reference spectra in the fuzzy classification.....	64
Figure 30 Graphical representation of spectral signatures in the HYPERCUBE library (grass in green, concrete in blue, and asphalt in black).....	65
Figure 31 Graphical representation of spectral signatures in the ASD library (vegetation in green, concrete in blue, and asphalt in black).....	66
Figure 32 List of spectral signatures from ASD library	67
Figure 33 Example of output image after running the shape similarity metric testing for a reference spectral signature representing grass from ASD spectral library (light shades of grey indicate pixels that are more likely to resemble grass, while darker shades are less likely to resemble grass)	69
Figure 34 Description of the three possible zones in a fuzzy set A, where a is in the set, b is outside the boundaries of the set, and c is in the fuzzy boundary of the set (source: Ross 2010).....	71
Figure 35 Membership values ($\mu(x)$) based on the boundaries of a set belonging to a fuzzy classification (source: Ross 2010)	72
Figure 36 Schema of the fuzzy classification with set boundaries for the shape and the distance criteria	73
Figure 37 Schema representing the combination of both shape and distance criterion for the fuzzy classification.....	74
Figure 38 Comparison of spectral signatures representing Asphaltic concrete (taken from ASTER spectral library), Concrete (taken from Hypercube spectral library), and Concrete medium (taken from the handheld ASD spectroradiometer spectral library).....	84
Figure 39 Interpolation of reflectance values at CASI 1500 wavelengths with HYPERCUBE spectral library	86
Figure 40 Distance similarity metric pitfall.....	88

List of Abbreviations

Abbreviation	Meaning
ASTER	Advanced Spaceborn Thermal Emission and Reflection Radiometer
CASI	Compact Airborne Spectrographic Imager
CMM	Communauté Métropolitaine de Montréal
DEM	Digital Elevation Model
EM	Electromagnetic
FWHM	Full Width at Half Maximum
HSS	Hyperspectral Scanner System
JHU	John Hopkins University
JPL	Jet Propulsion Laboratory
MLC	Maximum Likelihood Classifier
MNF	Minimum Noise Fraction Transformation
MSAS	Modified Spectral Angle Similarity
NIR	Near Infrared
PCA	Principal Component Analysis
ROI	Region of Interest
RF	Random Forest
RGBI sensor	Red, Blue, Green, Infrared sensor
SAM	Spectral Angle Mapper
SVM	Support Vector Machine
USGS	United States Geological Survey
VNIR	Visible and Near Infrared
WAAS	Wide Area Augmentation System

Acknowledgement

I would like to thank my supervisor, François Cavayas, for guiding me through this research project. I would also like to thank my family, in particular my brother Kiran who helped me collect field data.

Chapter 1 - Introduction

1. Context and problem statement

1.1. Urban planning and management

With an increasing number of people living in cities, urban management and planning is important to insure a good quality of life in urban areas. According to a (United Nations, Department of Economic and Social Affairs, and Population Division 2014) urban populations reached 3.9 billion people worldwide. This number is projected to increase to 6 billion people by 2045. To accommodate the constant inflow of people towards cities, urban planners need adequate tools and data to properly plan and manage cities.

Many facets of urban life are considered to maintain or increase quality of life in a bustling city. Urban areas can be summarily defined as a landscape that is dominated by infrastructure where a large population exists, that works primarily in non-agricultural employment(Breckenkamp et al. 2015). These areas need to be organized to accommodate an ever-growing population; large infrastructure developments like residential areas, industrial area, and transportation; and linkages between infrastructure and the environment(Waddell 2002). Understanding the structure of urban like land use, or the material composition of the urban landscape, is important for many overarching urban planning and management agendas.

With climate change, global temperatures seem to increase, and urban areas are not exempt from this phenomenon. Temperatures are regulated in part by the types of materials found in cities. Often, in areas where there is little to no vegetation, temperatures are much higher than areas where vegetation exists. With an accurate cartography of urban surface materials, city planners can determine where temperatures are likely to be higher during heat waves and they can identify heat islands. Populations at risks of heat strokes can be warned to avoid these areas during heat waves. Once the heat islands have been identified, they can be the subject of temperature reduction efforts such as planting trees or demineralization.

Indeed, surface materials such as asphalt on roads, or, cement on sidewalks, or, even the grass and tree borders between roads and sidewalks, have a large influence on environmental factors in cities. This includes, among others, surface temperature, roughness and imperviousness. In turn, these will affect the quality of life of residents by regulating surface water flows, winds and air temperatures, air quality, and more intrinsic values of cities, like the aesthetic values of trees, health and social benefits of parks and natural areas(Tyrväinen et al. 2005).

The city of Montreal, Qc, Canada, is the second largest metropolitan area of Canada. It is the economic centre of the province and welcomes a large number of industries and professionals. It has been subject to flooding and increasing temperatures. Proper management of the city structure is vital to ensure a better quality of life to its residents. The City of Montreal does not have an accurate or up-to-date database of surface materials. Many of their projects require this database. For example, the mandate to green the city of Montreal by increasing canopy cover from 20% to 25% required them to know which planting sites needed to be demineralized. Most of their cartography identifies objects rather than materials, meaning that surface materials at planting sites was not available. There is a need for identifying surface materials in Montreal for better urban planning and management.

1.1. Problem statement

The composition of urban areas is a complicated and heterogeneous patchwork of different materials. Often, data on surface materials is acquired through fieldwork, which can be a tedious and time-consuming task. However, remote sensing can be a good alternative to this problem. It is the science of acquiring information at a distance on the Earth's surface. Remote sensing exploits the interactions between objects and solar radiation. It can provide a faster and more affordable method for detecting ground objects such as trees in urban areas on a multi-annual basis (Myeong, Nowak, and Duggin 2006). Once a proper methodology for identifying surface materials has been established, monitoring over time will be much easier.

1.2. Study objectives and hypotheses:

This research project aims to identify and map surface materials within an urban landscape to aid in city planning and management. More particularly, this study uses aerial hyperspectral images to identify surface materials, such as asphalt, cement, grass, and trees. Every ground object has in principle, a unique response to solar radiation that can be measured with hyperspectral imagery. This is a concept known as the spectral signatures.

The objectives of this study will therefore be:

1. Finding a correspondence between the type of surface cover material and its spectral signature within the images.
2. Developing a sound methodology to identify surface materials in urban landscapes, with high resolution hyperspectral aerial imagery.

The basic hypothesis for this study is that target objects have a unique spectral response measured with a hand-held hyperspectral sensor (spatial resolution of 1m and spectral range of 340-1050nm). It is then, possible to develop a methodology that can separate the objects based on this spectral response.

1.3. Thesis structure

This thesis is organized into six chapters. Chapter 2 is a literature review of the current research and methods within the field of hyperspectral imagery focused on identify surface materials. The third chapter explains some preliminary studies done in the context of a Research and Development project for the City of Montreal. The fourth chapter describes the main methodology used to identify urban surface materials with our images. It covers the study area and the methodology. We will also cover some preliminary analysis done earlier on in the project. Chapter 5, describes and discuss the results of our methodology for identifying urban surface materials. Finally, chapter 6, presents a general conclusion of the research project and suggests some improvements that could be the object of future research.

Chapter 2 - Urban remote sensing with hyperspectral images: background

2.1. Sensors types and resolutions for urban remote sensing

Remote sensing has seen huge technological advances in imaging sensor types and image resolutions. Aerial photography was the most common imagery acquired when remote sensing first started being used. Cameras were mounted onto airplanes, and aerial photos were for reconnoitering purposes, especially during the First and Second World War (Borengasser, Hungate, and Watkins 2008). During the Cold War, the Arms Race helped encourage scientific discoveries such as the exploitation of the infrared part of the spectrum, and the development of observation technology like satellites, and sensors. A well-known example is the Landsat series of satellite that were developed by NASA, and were first launched into space in 1972, starting with Landsat 1. The objective of this series of satellite was, and still is, to observe Earth's land masses and assess the quality of ecosystems, and the effects of land changes (Masek 2019). The last satellite of this series, the Landsat-8, has on board a multispectral sensor, which has spectral bands in the visible part of the spectrum as well as the near- and shortwave infrared, and a thermal infrared sensor. Over the years many satellites have been sent into orbits by different private and public organisms, equipped with wide range of sensors. Nonetheless, sensors have been consistently mounted on airplanes and other airborne technology such as drones.

Figure 1 illustrates the requirements in terms of spatial, temporal, radiometric, and spectral resolution of sensors in conjunction with different application fields. Examples of sensors, most of them onboard satellites, are also given.

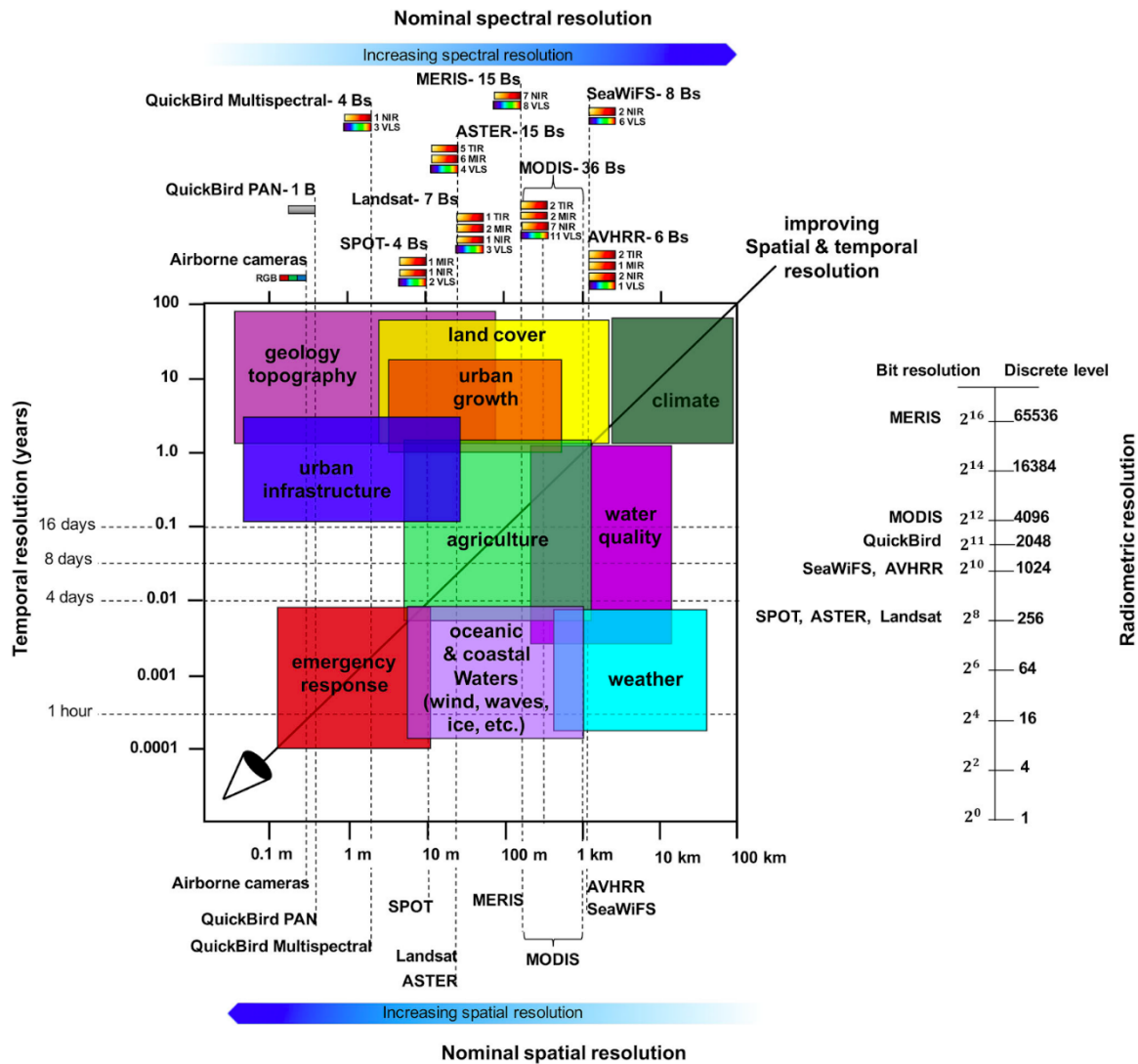


Figure 1 Graphical representation of sensors and their uses based on spatial, spectral, temporal, and radiometric resolution (source: Kadhim, Mourshed, and Bray 2016)

Spatial resolution can be defined as the smallest discernible object in an image. It is also defined as the area of one pixel (also known as unit) representing the same area on the Earth’s surface (Campbell 2007). As urban areas are extremely heterogeneous environments, spatial resolution is an important factor to consider when choosing the type of remotely sensed data for projects. Imagery with high (metric) to very high (sub-metric) spatial resolution is required to properly identify and understand urban landscapes (Longley 2002). In present days, space borne sensors like those onboard of Digital Globe satellites, provide imagery with metric (in multispectral mode) and sub-metric resolution (in panchromatic mode). Airborne sensors providing very high spatial resolution are often used in various infrastructure and vegetation surveys in urban areas and risk

or emergency response modeling (Kadhim et al. 2016; Myint et al. 2011). Figure 2 shows two images of the same urban scene taken at metric and centimetric spatial resolution. It is clear that with a finer resolution (figure 2.B), it is easier to trace the boundaries of different objects and to identify objects like cars, or patterns on the street than with the larger resolution (Figure 4. A).



A

B

Figure 2 Comparison of spatial resolution between two images of the same urban scene : A. an aerial imagery with 1m spatial resolution, and B. an aerial imagery with 25cm spatial resolution

Temporal resolution is the time lapse between each site visit. For satellites this is based on the orbital distances, while for aerial imagery, it depends on the time lapse between fly overs. Temporal resolution is a parameter to consider when performing urban growth and land cover change analysis which is not the case of our research project.

Radiometric resolution is the sensor's ability to store detailed information on signal intensity in numeric format. In other words, it dictates the levels of grey that can be separated when translating the received signal from objects to numeric values. Modern airborne or space borne sensors provide images with 16 bits pixel depth (65536 levels of grey). Radiometric resolution determines the amount of information stored in each image, and the capacity (time and effort) needed to analyze the imagery. Images with a lower radiometric resolution will take much less time to analyze than images with a high radiometric resolution. The trade-off is of course, the quantity of data that can be acquired.

Spectral resolution is another parameter to consider while choosing data for an urban study. Spectral resolution is the capacity of sensors to register the incoming signal in small wavelength intervals. It can also be defined as the narrowest spectral interval that can be resolved by a sensor (Campbell 2007). The term hyperspectral imager (or imaging spectroradiometer) describes any imaging sensor operating in the optical part of the electromagnetic (EM) spectrum and acquiring data with high spectral resolution. Images are then composed of many dozens of narrow and contiguous spectral bands. Contrary to hyperspectral sensors, multispectral imaging sensors acquire images usually composed by no more than ten spectral bands. For instance, the airborne sensor used in the present research, the CASI 1500 (Compact Airborne Spectrographic Imager), can be programmed to acquire data with up to 288 spectral bands between 350 and 1050 nm compared to 8 bands of the multispectral sensor onboard the Worldview satellites operating approximately in the same spectral interval.

Modern technology allows the development of both multispectral and hyperspectral sensors operating within the well-known atmospheric windows of the near UV (350-400 nm), the visible (400nm-700nm), the near infrared (700-1100), the short wave (1100 -3000) and mid wave infrared (3000-5000) as well as the far infrared (thermal infrared: 8000-14000nm) (Figure 3). Although spectral resolution is deemed less important than spatial resolution in urban remote sensing, it still holds an important role in image analysis (Myint et al. 2011). High spectral resolution allows spectral analysis of the components of an image, which in turn can help identify various objects based on their spectral signatures (Myint et al. 2011). Our focus is on hyperspectral images in the interval from near UV to NIR (Near infrared) as used in the present research. The next section describes in more detail the processing and analysis methods of hyperspectral images for extracting information on surface material cover.

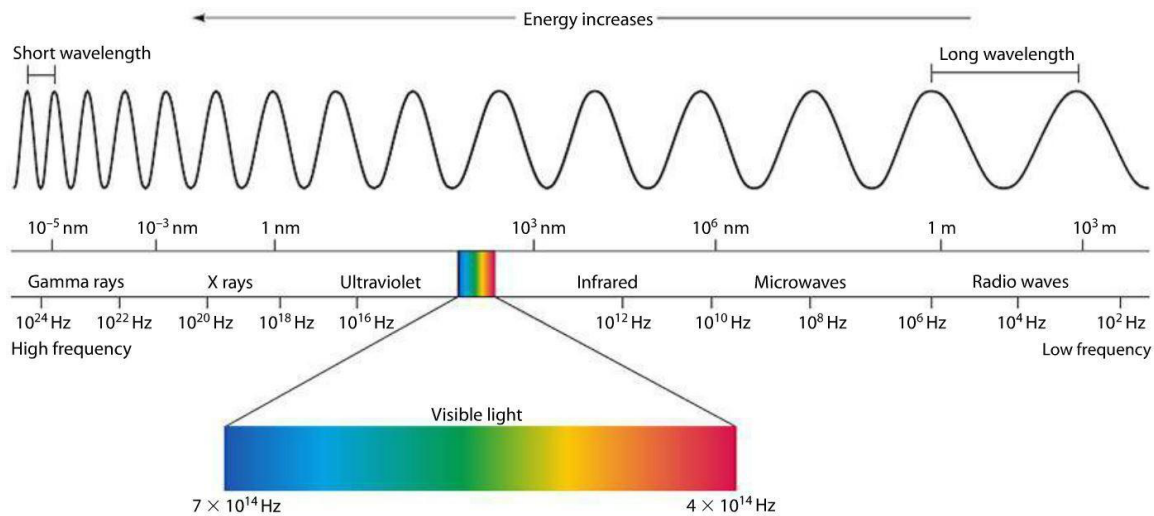


Figure 3 The electromagnetic spectrum

2.2. Hyperspectral imagery: processing and analysis

In the spectral interval of interest, hyperspectral images are created by capturing the solar energy reflected by a surface material and separating it into many spectral bands. The measured radiation per spectral band is expressed in radiance which is the radiant flux entering the sensor (Watt) per solid angle (steradian) of observation, per surface unit (m^2) projected in the viewing direction of the sensor and per wavelength (μm) (Figure 4).

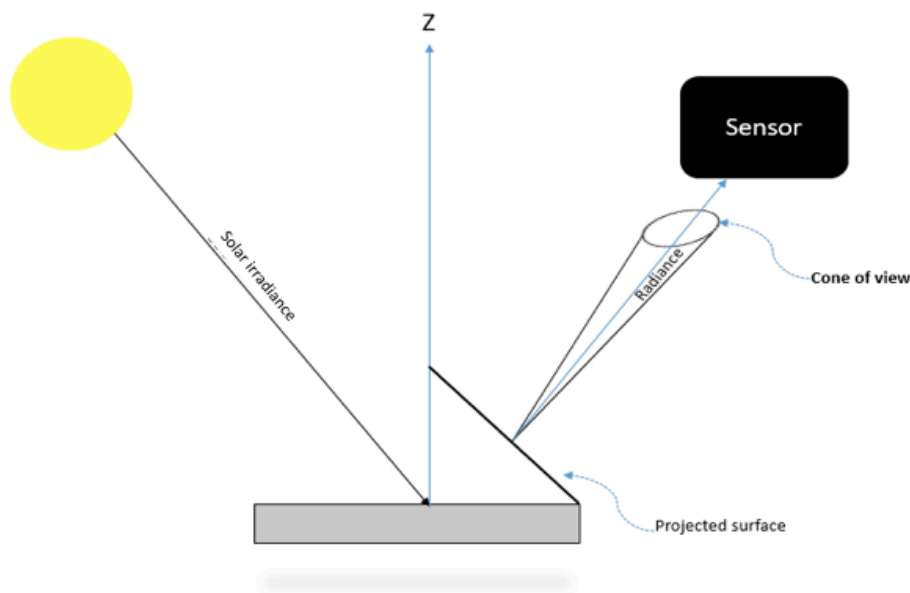


Figure 4 Diagram of radiance (adapted from Bonn and Guy 1993)

Hyperspectral data is often represented by a data cube (Figure 5). The x and y axis are the spatial axis, while the z axis represents the channels in which radiance measure are available (or the wavelengths the sensor was able to separate).

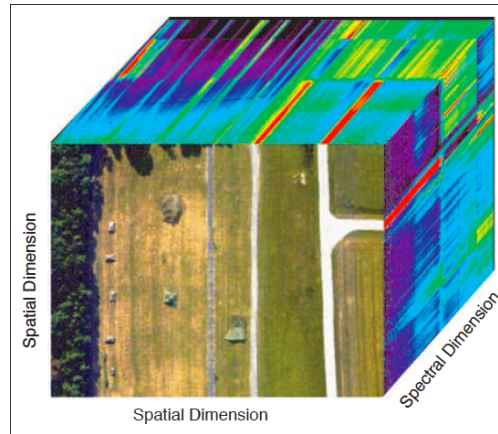


Figure 5 Hyperspectral data cube (source: Shaw and Manolakis 2002)

The apparent “spectral signature” (radiance values) per pixel shows clearly the potential of hyperspectral data to reconstruct the real spectral signature of a surface material (ground reflectance values) provided that atmospheric effects are corrected. In Figure 6, such an apparent spectral signature is drawn from our hyperspectral data set (see Chapter 3) with 96 bands. Radiation absorption effects of water vapour is evident in the NIR bands (band 50 and higher) with abrupt lowering of radiance values (hollows). The radiance values were provided to us with a multiplication factor of 1000. Conversion of measured radiance to ground reflectance is summarized in the next section.

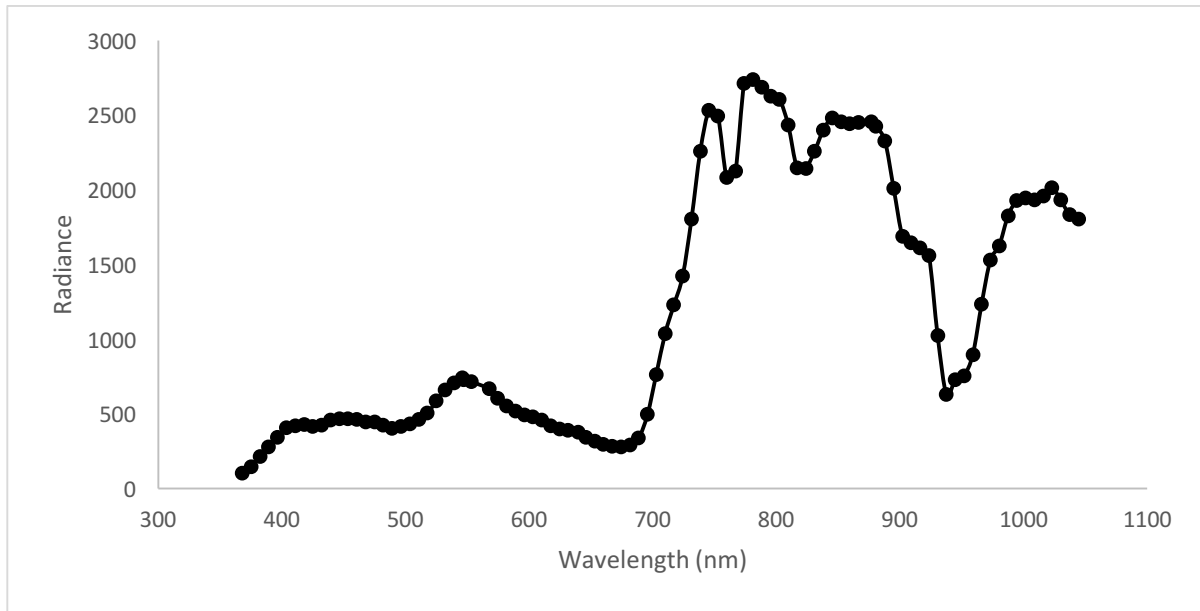


Figure 6 Apparent spectral signature in radiance units multiplied by a factor of 1000 of pixel covered by vegetation extracted from an airborne CASI1500 image (1m spatial resolution) with 96 bands between 350 nm and 1050 nm

Various techniques are used to identify surface materials based on their spectral signatures. Most of the times these techniques are based on reference signatures found in spectral libraries or extracted from the images themselves (endmembers). Section 2.2.2 presents a review of these techniques.

2.2.1 Extraction of spectral signatures

Reflectance is an inherent optical property of a surface material and has values between zero and one as it is the proportion of reflected energy over the total amount of radiation incoming for the sun. Reflectance varies from one wavelength to another depending on the physicochemical structure of the surface material. Variation of reflectance throughout the solar spectrum is termed spectral signature, a way to signify that, theoretically, such variations are unique and depends solely on the surface material. Hyperspectral images are a high-density spectral sampling of EM energy more able to reconstruct the spectral signature of a surface material than a multispectral sensor.

However, the EM energy measured by a hyperspectral sensor is not directly related to the spectral signature of a material. As mentioned, the reflected solar energy measured by the sensor in a spectral band, is radiance ($\text{W}/\text{m}^2/\text{sr}/\mu\text{m}$). Assuming a target reflects solar energy equally well in any direction (isotropic or Lambertian target), radiances vary not only with the reflectance of the examined targets but also depend on the atmospheric and solar illumination conditions during image acquisition. The incompatibility between radiance spectra and reflectance spectra is more important over urban areas where the atmosphere is usually loaded with gases and particulates (aerosol), which absorb and scatter solar radiation in various ways throughout the spectrum. As the particulates are usually concentrated in the troposphere, even in airborne imagery, as used in our study, atmospheric effects are almost always present. The airborne sensor has a wide field of view, atmospheric effects are not manifested in the same manner from one pixel to another.

In our laboratory, we have access to a computer program `ATMOCOR_CASI` (in C-Sharp; François Cavayas personal communication) adapted to the particular acquisition conditions of our set of images provided by the airborne sensor CASI1500 (see Chapter 4 for more details). The program makes use of the various routines freely available of the 6SV atmospheric code (Vermote et al. 1997) written in FORTRAN to simulate gas absorption as well molecular (Rayleigh) and aerosol (Mie) scattering effects in both the incoming and the outgoing radiation path by considering (a) a particular atmosphere stratification with specific populations of gases and aerosol particulates per layer; (b) a particular composition of the aerosol loading (dust, black carbon, water soluble, salts), (c) the solar position and the sensor viewing conditions during image acquisition; (d) the type of surface reflection: isotropic or anisotropic; and (e) the altitude of the terrain as well as the height of the sensor (airborne case). By fixing the above-mentioned parameters the program converts the image radiances into ground reflectances in two steps.

The first step is to convert measured radiances into apparent reflectance factor (Equation 1). Reflectance factor is the ratio of the radiance measured by the sensor to the radiance of a perfect Lambertian target measured under the same viewing and illumination conditions as the target:

$$\rho_{sensor}(\Delta\lambda, \theta_s, \theta_v, \varphi_s - \varphi_v) = \frac{\pi L(\Delta\lambda, \theta_s, \theta_v, \varphi_s - \varphi_v)}{\frac{E_0(\Delta\lambda)}{d^2} * \cos \theta_s} \quad (1.)$$

Where ρ_{sensor} is the reflectance at the sensor level at a spectral band $\Delta\lambda$, L is the measured luminance at the same band, $E_{\theta_{is}}$ the solar radiance at the top of the atmosphere for an average Earth-Sun distance (1 astronomical unit), $\cos \theta_s$ is the cosine of the sun zenithal angle θ_s , and d represents the distance between the Sun and the Earth at the moment of image acquisition (in astronomical units). In the above equation, all spectral quantities depend on the sun zenith angle (θ_s) and the sensor view zenith angle (θ_v) as well as on the relative azimuth between the sun and the sensor ($\varphi_s - \varphi_v$).

The second step is to correct apparent reflectance from atmospheric transmission and scattering effects. According to Vermote et al. (1997), under the assumptions of Lambertian target of infinite extent and a complete independence between atmospheric transmission and scattering, the apparent reflectance can be written as:

$$\rho_{sensor}(\Delta\lambda, \theta_s, \theta_v, \varphi_s - \varphi_v) = T_g(\theta_s, \theta_v) \left[\rho_{R+A} + T^\downarrow(\theta_s)T^\uparrow(\theta_v) \frac{\rho_{target}}{1 - S\rho_{target}} \right] \quad (2.)$$

For which, $T_g(\theta_s, \theta_v)$ is the transmission of gases (e.g. H₂O, CO₂, O₂, and O₃), ρ_{R+A} is the reflectance of the atmosphere due to Rayleigh and aerosol scattering, $T^\downarrow(\theta_s)$ represent incoming atmospheric transmission due to scattering (between the sun and the ground), and $T^\uparrow(\theta_v)$ represent the reflected atmospheric transmission due to scattering (between the ground and the sensor); ρ_{target} represents the ground reflectance factor for a Lambertian target. The expression $\frac{\rho_{target}}{1 - S\rho_{target}}$ represents the radiation reflected by the infinite target after many interactions between the target and the atmosphere with spherical albedo S . Radiation quantities depend on the position of the sun and the sensor viewing conditions. Chapter 4 presents in more details the way that the various parameters were fixed in the particular case of the images used in the present study.

2.2.2 Identification of surface cover materials

In general, two main approaches are used to identify surface cover materials. The first one is an adaptation of classification algorithms developed for multispectral image analysis to the hyperspectral images. The second approach is based on the comparison of reference spectral signatures of the searched materials, usually extracted from external reflectance libraries, to the observed spectral signatures on the image. A third approach is also followed, usually with images of metric spatial resolution. In that case, reference spectra are used to establish the proportion of the surface of a pixel occupied by the reference materials (unmixing). These approaches are examined in the next paragraphs.

2.2.2.1 Classification algorithms

Many classification algorithms can be used to distinguish between surface cover materials on a pixel or a region (object) basis. Priya and Murugan (2013), present a general review of these algorithms. Usually the first step is to reduce the dimensionality of the hyperspectral data set given the redundancy in the information content of many spectral bands. Algorithms such as PCA (principal component analysis) or the MNF (minimum noise fraction transformation) are applied. Then training sites are selected and supervised algorithms are applied to the reduced image set. The study of Burai et al. (2015), in a complex rural environment, is a typical example of application of such algorithms with hyperspectral airborne images. The 128 original spectral bands in the 400-1000 nm (AISA sensor) were combined to create a dozen of bands with the MNF algorithm and used with three supervised classifications algorithms: the MLC (maximum likelihood), the SVM (support vector machine) and the RF (random forest) to identify 20 vegetation classes. All the algorithms were accurate enough (>80%) with 20 classes. The accuracy rises (> 95%) when the 20 classes are grouped to form 5 vegetation groups. While the SVM and RF algorithms can be applied with the original data set because their performance does not depend on the number of the training sites, the MLC is inapplicable in practice with the original data sets because, as the author demonstrate, his performance is heavily dependent on the number of training sites. With the image set of 128 spectral bands there is a need of at least 129 training sites.

The study of Chisense (2012), is another example of adapting the approaches used in the analysis of multispectral images to hyperspectral images. The author is interested on the identification of roof materials of buildings in a city in Germany. He uses the images of the airborne HyMap sensor

with 125 bands in the interval from 400 nm to 2500 nm (4 m of ground sampled distance). The building roofs are isolated using external data, an unsupervised classification algorithm (ISODATA) is then applied in order to extract training sites corresponding to 10 classes of roof material. After dimensionality reduction, the new image set is segmented into homogeneous areas and each area classified by a maximum likelihood object classifier. The obtained results are significantly accurate.

More sophisticated approaches are also proposed using variances of the C-fuzzy classification, neural networks, neuro-fuzzy networks, etc. (e.g. Kakhani and Mokhtarzade 2019). However even with such sophisticated approaches the number of identified surface materials (or land cover classes) are not significantly different from those identified with less sophisticated methods (and far less time-consuming approaches).

2.2.2.2 Use of reference spectral signatures

These approaches use similarity metrics between a reference spectral signature and an observed spectral signature on a pixel basis. The Spectral Angle Mapper, also known as SAM, is a classic example of this type of approach. The algorithm calculates the angle between the reference spectral signature and the image spectral signature. To accomplish this, spectral signatures are assumed to be vectors of n -dimensions (n -dimensions equal the number of bands within the image). The smaller the angle, the more similar the two spectral signatures are. A threshold value determines if their similarity is acceptable for a given class. Kruse et al. (1993), use the following formula (Equation 3) to describe the angle calculation:

$$\alpha = \cos^{-1} \left[\frac{\sum_{i=1}^{nb} t_i r_i}{\sqrt{\sum_{i=1}^{nb} t_i^2} \sqrt{\sum_{i=1}^{nb} r_i^2}} \right] \quad (3.)$$

where nb is the number of bands in the image, t is the image spectrum at pixel i , r is the reference spectrum, and α is the angle between the two spectra in radiance.

Certain authors prefer the use of the Modified Spectral Angle Similarity (MSAS) than simply the angle between the two spectra, as it has values between 0 and 2 (Homayouni and Roux 2004):

$$MSAS = \frac{2\alpha}{\pi} \quad (4.)$$

where MSAS is the modified spectral angle similarity, α is the angle between the reference spectrum and the image spectrum in radiance units.

Reference spectra can be found in spectral libraries such the NASA's ASTER (Advanced Spaceborn Thermal Emission and Reflection Radiometer) library (Meerdink et al. 2019) or developed with *in situ* observations with handheld spectroradiometers. While existing spectral libraries are developed with laboratory measurements, *in situ* observations offer a better support as adapted to the materials present in a particular study area.

The use of SAM in urban areas has shown some success. As an example, Moreira and Galvão (2010) were interested in impervious surface materials identification in Sao Paulo, Brazil, with hyperspectral data. Their methods compared reference spectra from field surveys, done with a spectroradiometer, to pixel spectra from a hyperspectral aerial sensor, the airborne hyperspectral scanner system (HSS), with 2.7m spatial resolution and 37 spectral bands in the visible and near infrared portions of the EM spectrum. They found that overall accuracy of SAM classifier using all bands was 74%.

When using SAM for classification, a user defined threshold is used to classify image pixels based on their spectral angle between image spectrum and reference spectrum. The smaller the angle, the more likely the two spectra are similar. Mohammadi (2012) found that using a smaller threshold value made SAM classification more accurate. In his study that aimed to classify roads and assess their conditions, he used hyperspectral imagery, taken over Baden-Württemberg (Germany), to find asphalt, concrete, and gravel. A flaw he found with SAM, was the large number of unclassified pixels. With a low threshold value, many calculated angles between reference and pixel were too large to be classified in an appropriate class; resulting in many unclassified pixels.

Other studies show different accuracy levels for SAM classifiers. A study in China that used aerial hyperspectral and satellite hyperspectral imagery to identify hazardous surface materials had an 86% success rate, compared to only a 65% success rate using different spectral image classifier (Ye et al. 2017). The authors also found that the optimal threshold angle changed depending on the type of material that needed to be identified. For example, recognizing steel rooftops with SAM was best accomplished with a threshold angle of 0.25 radians, while identifying roads made of asphalt was easier when using threshold of 0.1 radians. Overall, the study found that SAM had potential for material identification in urban areas. However, a study that aimed to identify tree species in a forested area with hyperspectral imagery of 1m resolution only found that SAM had an overall accuracy of 48.83%. Other classifiers used in the study had a much better accuracy level, going up to 85.56% when using MLC (Shafri, Suhaili, and Mansor 2007). One of the differences between these two studies is the area of study. One study looks at an urban area with many types of materials with spectral signatures that have different shapes, while the other tried to differentiate between tree species that have more or less the same shape. The SAM algorithm was not well suited for differentiating between spectral signatures that had the same shape such as tropical tree species.

2.2.2.3 Unmixing

As remotely sensed urban scenes are characterized by heterogeneous materials in close proximity and or adjacent to one another, often pixels found within the image are considered mixed. That is to say mixed pixels are pixel that hold more than one material in varying proportions. There are two common reasons for mixed pixels to occur, the first is that spatial resolution of an image. If the spatial resolution is too low, multiple objects can be represented in one pixel. For example, if a pixel of 5m is at the border between a sidewalk and a garden, then the pixel will have spectral signatures of both grass, and cement. The second reason mixed pixels occur is when the nature of the material itself is mixed. For example, a pixel representing a piece of road is composed of all the materials that go into making an asphalt road which are asphalt, cement, rocks, etc. (Keshava and Mustard 2002).

In order to deal with mixed pixels, spectral unmixing algorithms were developed. In hyperspectral data, the high spectral resolution allows the identification of different spectra representing the varied materials in each mixed pixel (also known as mixels). Figure 7 illustrates this idea with a hyperspectral data cube. In fact, the pixel's spectral signature can be thought of as a weighed combination of unique spectral signatures of materials present on the ground at the location of said pixel. The combination is simplified to a linear relationship mathematically represented by equation 5:

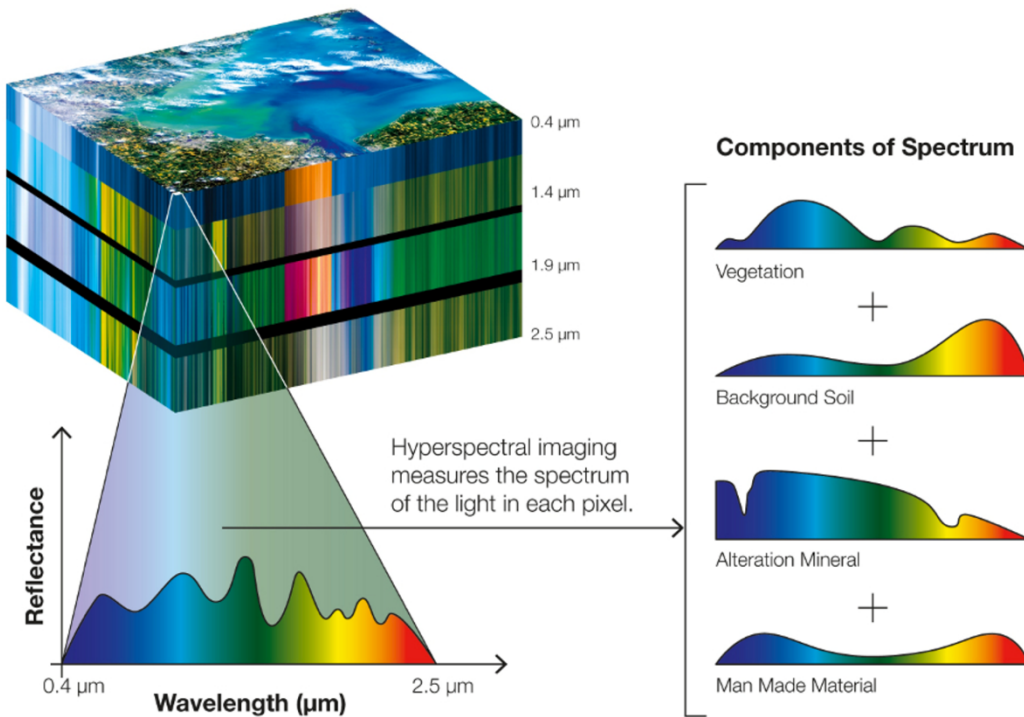


Figure 7 Schema of a mixed pixels and the linear combination of the spectral signatures it is composed of vegetation, background soil, minerals, and manmade materials (Source: Geo University, website: <https://www.geo.university/courses/the-network-based-method-spectral-unmixing-framework>)

$$\rho[\lambda]=s_1\rho_1[\lambda] + s_2\rho_2[\lambda] + \dots + s_n\rho_n [\lambda] \quad (5.)$$

with $\rho[\lambda]$ the reflectance of a pixel at wavelength λ , s_n the proportion of each distinct object with reflectance ρ_n .

Linear unmixing models suppose that each radiative interaction is unique by the time it has reached the sensor. This assumption is often criticized as photons tend to interact with many objects and bounce off a multitude of materials. To account for these multiple interactions, nonlinear models were created. However, when considering non-linear unmixing, it is very difficult to model multiple light interactions, as the properties change with the smallest disruption to the light's initial path (Dobigeon et al. 2014). Figure 8 shows bidirectional interactions of photons with the surface of the Earth, one of the many possible non-linear interactions. Equation 6 describes nonlinear models (Plaza et al. 2007),

$$r = f(E, \alpha) + n \quad (6.)$$

where $f(E, \alpha)$ represents a nonlinear function describing the relationship between E and α , and n represents the correction factor for noise in the image.

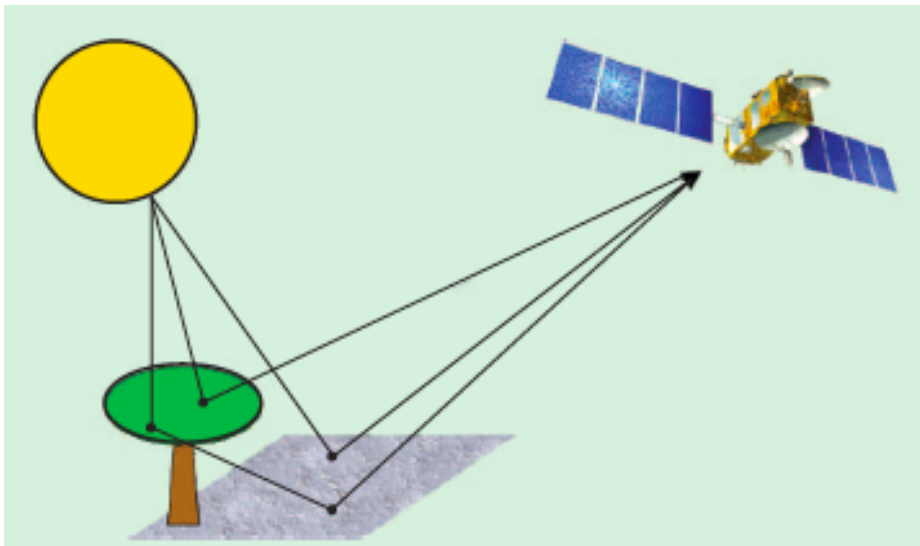


Figure 8 Interactions of photons causing a non-linearly mixed pixel (source: Dobigeon et al. 2014)

Heiden et al. (2001) have done many studies to classify urban surface material in Dresden, Germany. They use the airborne sensor HyMap data, with 6m resolution and 128 spectral bands ranging from the visible to the shortwave infrared. As noted earlier most urban remote sensing studies are accomplished with sub-metric spatial resolution, however, this is only in more recent

studies as the technology has improved. In the early 2000's most studies were done with resolutions under 10m. Heiden et al. (2001) study aimed to create a detailed spectral library of urban materials based on a predetermined subdivision by infrastructure types. The second objective of the study was to identify surface materials based on their spectral characteristics. In order to do this, they performed spectral unmixing techniques to account for mixed pixels. Their method was very successful and reached 99.8% classification of the area, more than half of which was composed of mixed pixels. As each spectral signature has a unique shape and can be identified by its discrete absorption features, Heiden et al. (2001), ascertain that a robust spectral library can greatly improve the ability to successfully classify urban areas.

Some studies have found that using a combination of different classifiers helps increase accuracy levels. Indeed, Segl et al. (2003) found that finding image feature based on shape (or shaped base feature identification algorithms), helped differentiate between objects commonly found in urban areas such as buildings, open areas, etc. Once there "shapes" were found, seedling pixels could be assigned more precisely. Seedling pixels are pixels that are spectrally pure, similar to the endmember concept. Once seedling pixels were identified, an unmixing algorithm was performed on the urban study area. They compared the success rate for identifying surface materials using only spectral unmixing and shape. They found that using a combined methodology helped to better differentiate between materials and increased accuracy.

2.3 Partial conclusions

Identifying surface cover materials in urban areas using hyperspectral imagery is a challenging operation. Until today there is not a clear indication in the way to attack this problem. Our data set is composed by images of one meter spatial resolution (see next chapter). So, mixed pixels should be present and linear unmixing approach is a simple and interesting way to address the material identification problem. The other approach we decided to follow is to develop similarity metrics between reference and observed spectral signatures such as the shape metric and an approach to decide to the degree of similarity which is independent of thresholds.

Chapter 3 - Preliminary studies

This chapter is an overview of the preliminary analysis performed to identify urban surface materials. In the context of a Research and Development project with the City of Montreal, we performed a series of preliminary analysis on our CASI images. The goal of the project was to develop a methodology to identify urban surface materials to aid with planting efforts in Montreal. The City of Montreal had a mandate to green the city by increasing the greenness index from 20% to 25%. In order to accomplish this goal, they wanted to plant trees on public property throughout the city. However, removing asphalt, concrete, or other building materials can incur an enormous cost. Therefore, they needed to know the scope of this greening project by having a detailed database on urban surface materials in Montreal. They could have acquired this information with field surveys but to cover the entire island would have demanded a large mobilisation of personnel and resources. Remote sensing of urban materials offered them an alternative to field surveys.

The city completed a theoretical exercise in which geomatics professionals created a sample of 1265 geo-located points where trees could potentially be planted on public property (e.g. sidewalks) free of any structure (e.g. lamps, bus stops). They needed a way to find out if these potential locations were in a state to be immediately be planted in (e.g. bare soil or grass cover), or if site preparation was needed before planting (e.g. cement or asphalt removal). In the last case, this would incur larger costs, and more time for the plantation efforts.

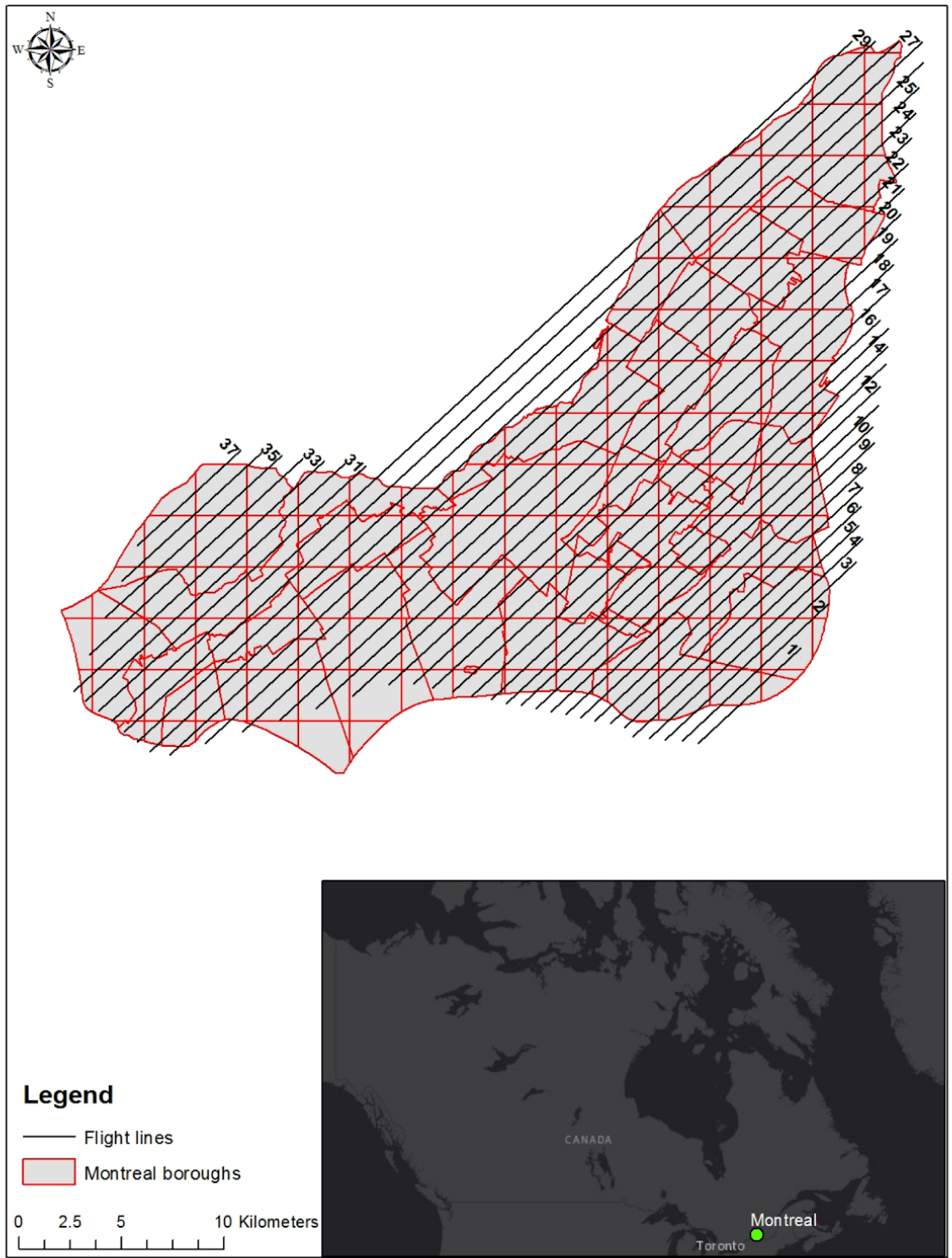
The city of Montreal also provided us with field points for which surface materials had been identified. These points were geo-located and solely situated on public property. They were used as validation points for the methodology.

This chapter is divided into two sections. The first section describes the methodology to identify urban surface materials using the CASI 1500 images. While the second section describes some tests made with the multispectral high-resolution aerial imagery taken with a VEXCEL- VNIR

(visible and near infrared) camera. This second section permits us to assess the potential of using sub-metric imagery for urban studies as opposed to the metric CASI 1500 imagery.

3.1. CASI imagery analysis

Our experiment was based on airborne hyperspectral imagery acquired by the City of Montreal in the summer 2016 covering the entire Montreal Island. The sensor was CASI 1500 operated by the company ITRES (Calgary, Canada). Figure 9 shows the flight lines followed over the city to obtain the images. These were separated into two zones, the first where the flight lines overlapped by 50%, the second where the flight lines overlapped by 35%. The flight line overlap changes to account for changing topography and tall buildings. The altitude of the flight lines varies between 887 m and 914.8 m. Due to adverse atmospheric conditions, the coverage of the whole Island spread at different times in August and early September and were acquired between 13:00 and 16:00. The frame time was fixed to 18ms. The images had a 1m spatial resolution and a spectral resolution of 96 contiguous bands spanning between 380 nm and 1040nm with a bandwidth of 7.2 nm. That is to say, the images cover the visible portion of the EM spectrum as well as most of the NIR, with band intervals approximately 5 nm in width.



WGS_84_UTM_zone_18N

7th of May 2019

Producer: Meghana Paranjape

Figure 9 Study area with flight lines of CASI 1500 hyperspectral aerial imagery

The study area for these preliminary analyses was the borough of Montreal North (Figure 10). This borough has a very heterogeneous landscape and lacks a lot of greenery. That is why city officials thought it would be a good place to issue a priority planting mandate. Montreal North is an area with large industrial zones composed of building materials such as asphalt and cement. Most of these industrial zones have large parking lots associated with them, which increases the built portion of the borough. Residential areas cover a large area of the borough and clearly have more greenery than commercial or industrial zones. The following figure shows an overview of Montreal North, with flight lines that went through it. One can also see, that the CASI imagery shows many grey buildings (built materials), and little or sparse greenery (or vegetation).



Figure 10 The borough of Montreal North: mosaic of CASI 1500 hyperspectral imagery (true color composite bands 14 in blue, 28 in green, and 42 in red) with the flight lines covering it

As the images cover an urban area with 1m spatial resolution, pixels often covered an area with many materials, and would be considered mixed pixels. Therefore, we decided that linear spectral unmixing would be suitable for this initial analysis. As explained in equation 5, linear spectral unmixing supposes that a pixel's spectral signature is the weighted combination of spectral

signatures of the materials that can be found within that pixel. To ease computational needs of the study we limited our tests to public property.

3.1.1. Methodology of preliminary study with CASI 1500 imagery

Figure 11 is a flowchart of the preliminary methodology used to identify urban surface materials with the CASI 1500 images. The first step of the methodology was to convert our images from radiance to reflectance. Then, we needed to find our regions of interest which were used as the reference spectra to run the linear spectral unmixing algorithms. Finally, these unmixing results were classified to obtain a final cartography of surface materials in Montreal North. This classification was validated with the geo-located points provided by the City of Montreal. These steps are described in more detail in the next paragraphs.

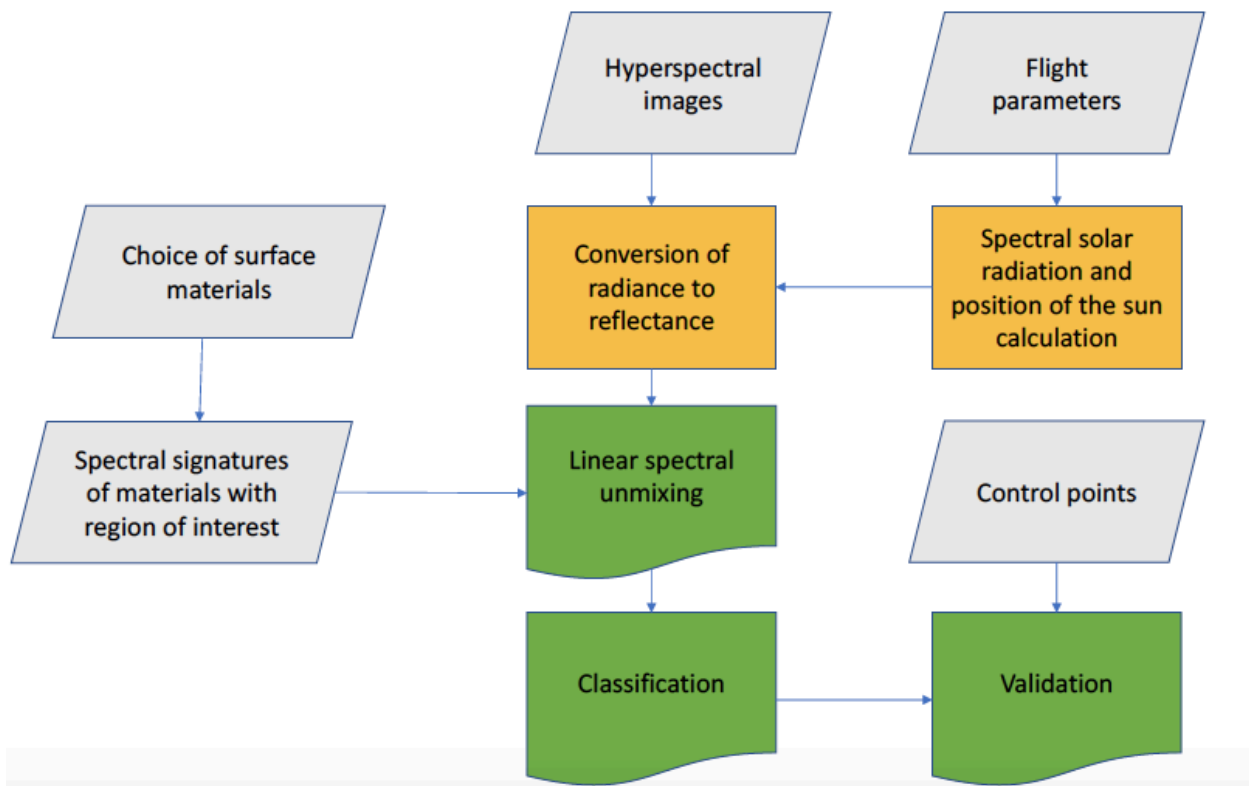


Figure 11 Flowchart of preliminary analysis to identify urban surface materials using linear spectral unmixing

The aerial images were provided to us in radiance units. We converted the radiances into apparent reflectance using the flight parameters, the position of the sun during acquisition, as well as the spectral solar radiation. Equation 1 describes the conversion formula (see Chapter 2). Usually, after this first conversion, we would need to perform atmospheric corrections to obtain object ground reflectance. However, at this stage in our study we had not created the atmospheric corrections algorithm used in the rest of the study (see Chapter 4). Therefore, we proceeded with apparent reflectance for the spectral unmixing algorithms.

3.1.2. Spectral unmixing

3.1.2.1. Reference spectral signature

The City of Montreal wanted us to identify were asphalt, concrete, cobblestone, low vegetation, and other inert materials. Spectral signatures for these materials can be found in spectral libraries measured with *in situ* methodologies using spectroradiometers. However, because the images were not yet atmospherically corrected, it was not possible to use spectral libraries as reference spectra. Instead, we used pixels within the image that contained only one material. These pixels are ‘pure’ pixels and are used as ‘endmembers’ and are input as reference spectra in our study.

We found these pure pixels using the region of interest (ROI) method. ROIs provide an average spectral signature for every material of interest. They are contiguous groups of pixels throughout the image grouped into polygon representing one type of material. By taking ROI’s throughout the image, we can take into consideration some illumination variation. We can also take into consideration the variability of the spectral signature of the same type of material. Figure 12 gives an example of the spectral signatures possible of asphalt and concrete.

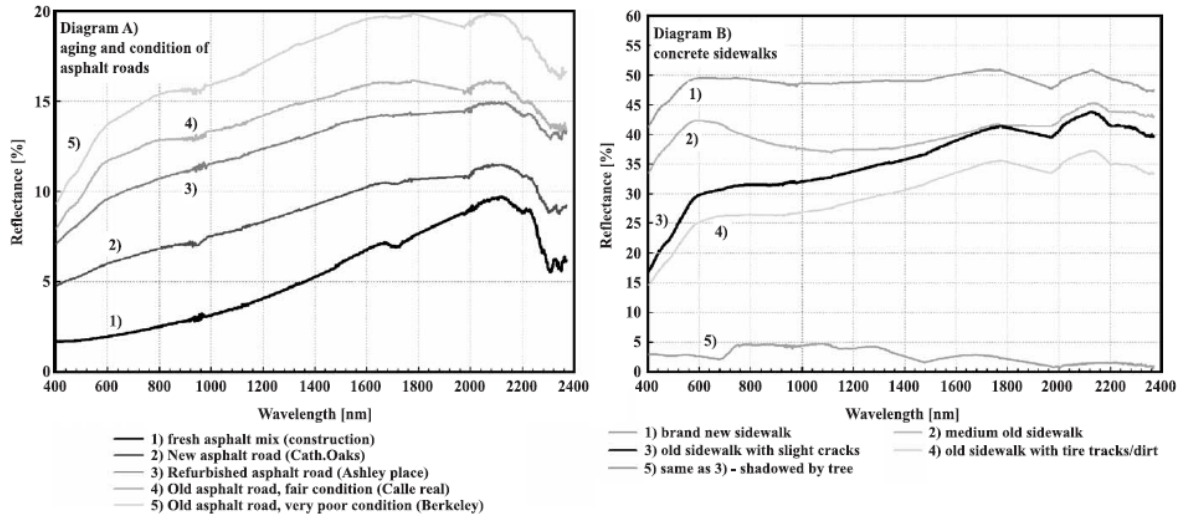


Figure 12 Spectral signatures of asphalt and concrete (between 440nm and 2400nm) (source: Herold et al. 2004)

3.1.2.2. Unmixing and Classification

These average spectral signatures were used to run a linear spectral unmixing algorithms. The results we obtained were one new image for each type of material we had chosen to separate. For each pixel, we had the proportion of the material that could be found in it. Some examples are shown in figures 13 to 15.

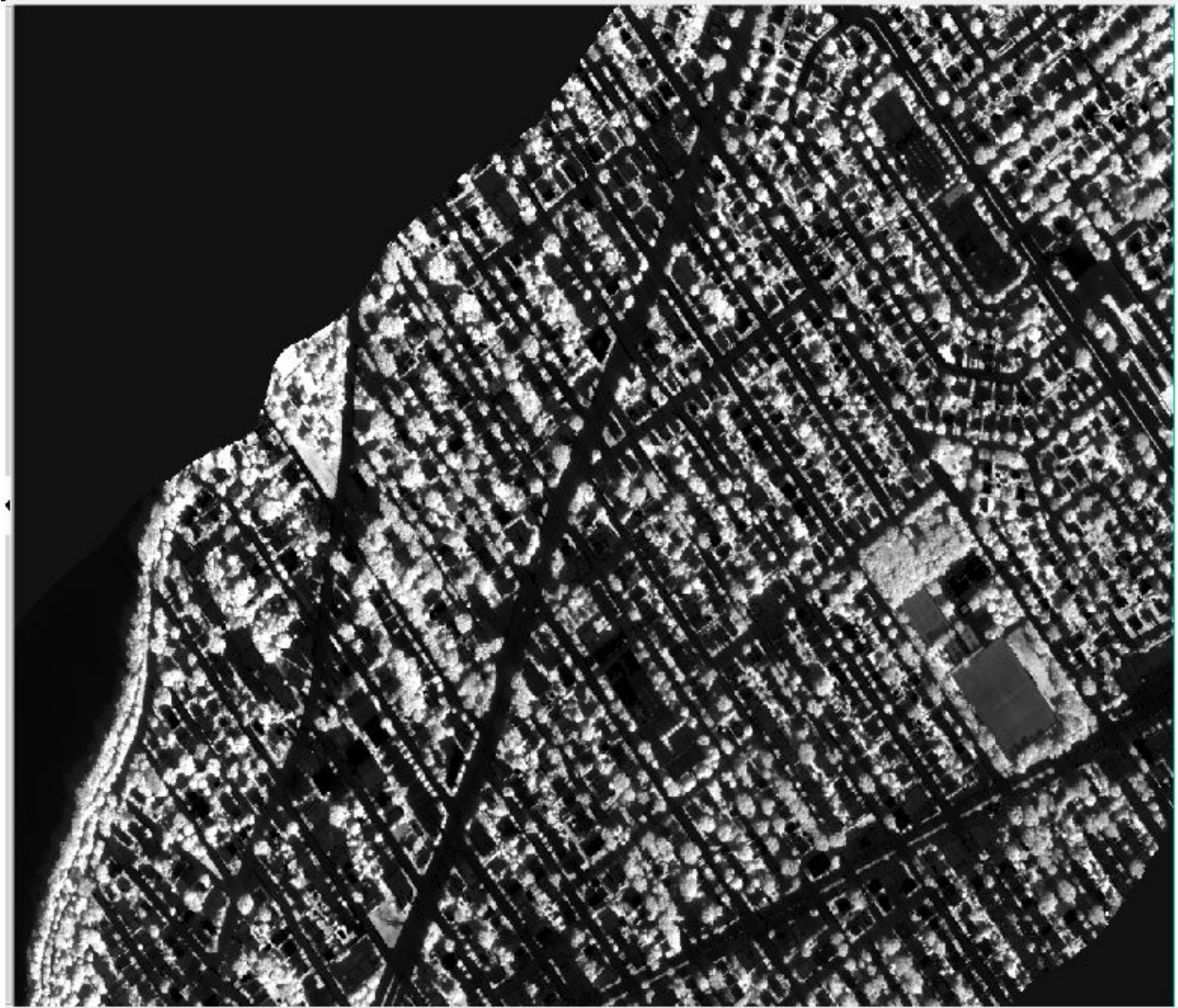


Figure 13 Linear spectral unmixing results using hyperspectral CASI 1500 imagery of Montreal North (Montreal, Qc, Canada), bright shades represent higher proportions of vegetation, while dark shades represent lower portions of vegetation



Figure 14 Linear spectral unmixing results using hyperspectral CASI 1500 imagery of Montreal North (Montreal, Qc, Canada), bright shades represent higher proportions of asphalt, while dark shades represent lower portions of asphalt



Figure 15 Linear spectral unmixing results using hyperspectral CASI 1500 imagery of Montreal North (Montreal, Qc, Canada), bright shades represent higher proportions of concrete, while dark shades represent lower portions of concrete

Finally, we had to classify the results of our spectral unmixing. For this we used a binary decision tree to create 46 classes based on the variability statistics of each image after unmixing. The 46 classes gave us an idea of the proportion of target materials in pixels. In order to simplify validation efforts, we grouped these 46 classes into 4 overarching classes by visual interpretation of the images. The four classes were asphalt, concrete, vegetation, and other. If the pixel had equal to low proportion of one or many materials than it was classified into the category it appeared to be by photo-interpretation. We also created a much simpler classification that classified the pixels by the material that had the largest proportion in each pixel. This lead to an end classification with 4 classes: asphalt, concrete, vegetation, and other. This second classification was not subject to photo-interpretation errors. It simply took the material that had the largest proportion in each pixel as the final classification.

3.1.3. Results and discussion

We validated the classification using the potential planting points for which the ground surface materials were known. A sample of 185 points were used that covered the study area. For both types of classification, the results were less than optimal, reaching overall success rates of 49% and 55%. In light of these poor results, we tried to find sources of errors.

First, we decided to reclassify the pixels with a modal filter with a window of 3 x 3. With this filter, the central pixel would take the most prolific value of the 9 pixels in the 3x3 window. An example is given in figure 16: the central pixel has a value of 1 and would be transformed into a value of 2 by the modal filter, as the value of 2 is the most common value in the 3x3 window. The results of the classifications were slightly better but still low, reaching overall success rates of less than 60%. About 40% of the total number of pixels that fell under the 1265 theoretical planting points for which surface materials were known, changed values after the filter was used. This indicates that the points fall in areas of transition for which dominant material identification is less certain.

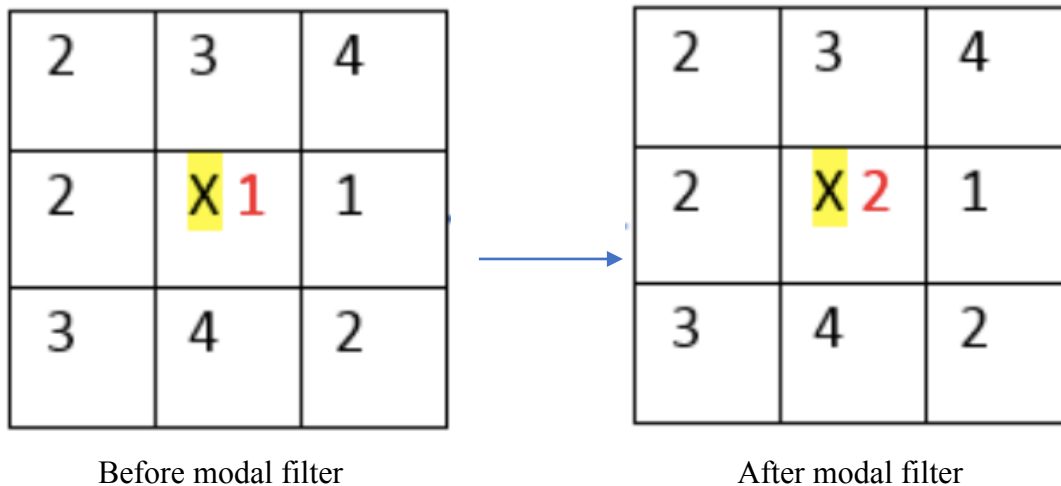


Figure 16 Modal filter

Another source of error could have been the fact that certain points did not correctly fall in their geographic positioning (Figure 17). This may be due to the inherent error in orthorectification of the hyperspectral images. It may also be due to the error associated with point's acquisition

method. Indeed, the points were taken with satellite and GPS technology in differential mode with the WAAS correction system. The error in geolocation is between 0.50m and 1m for 1 standard deviation. If we were to take a confidence interval of 95%, ($\sigma=1.96$), then the positioning error would increase to $\pm 3.3m$. A clear example of this error is illustrated in the following image (figure 18) for which the pixels under the points were classified as asphalt, which seems correct by photo-interpretation. However, field inventory of these points was said to be 'ready to plant', meaning they should have been located on the grass about three pixels to the right of their current location.

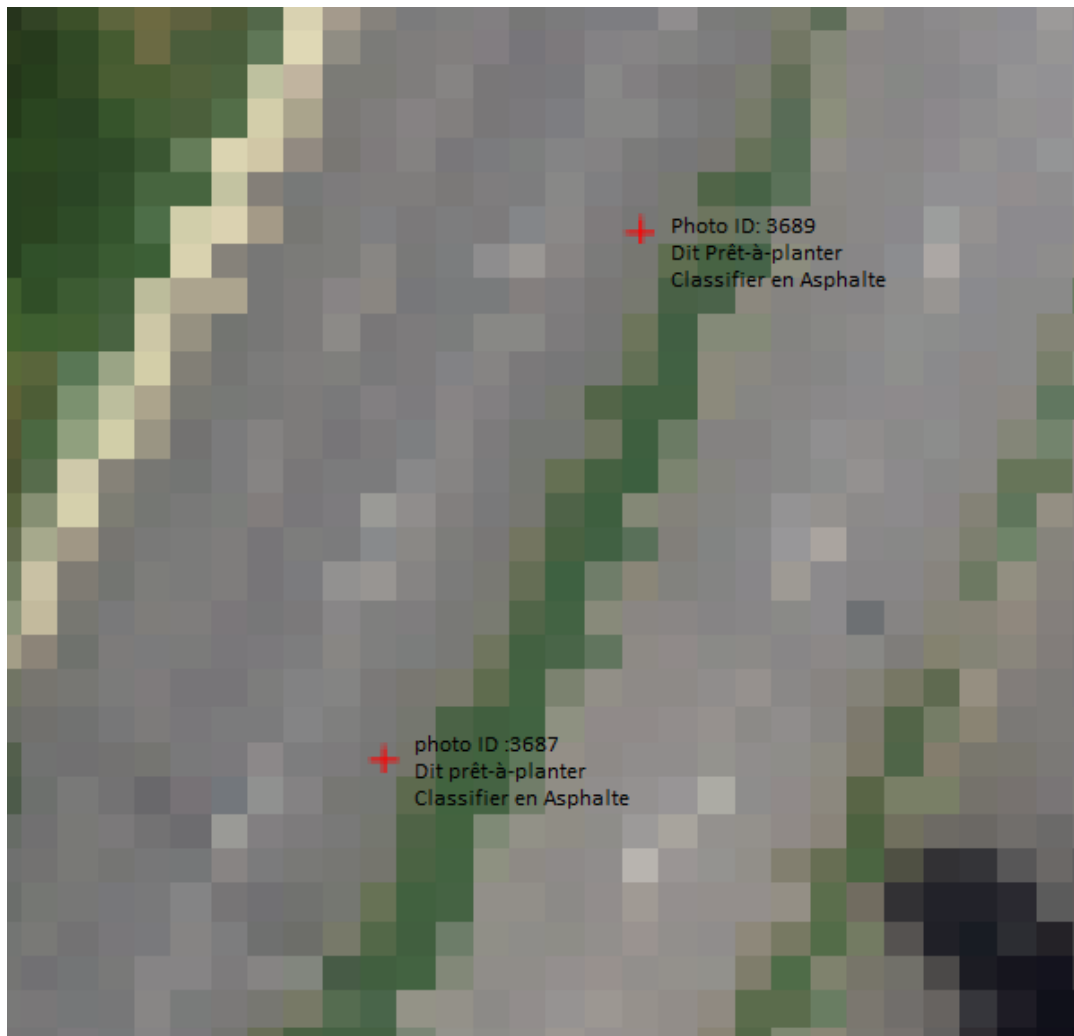


Figure 17 Miss-positioning of validation points: two points said to be 'ready to plant' falling on an asphalt road

The last source of error we thought could have affected the results was shadowed areas. When pixels fall under shadowed areas from buildings or canopy, it is much harder to obtain a spectral

response from them. This low spectral response could have led to errors during classification. We decided to test if excluding shadowed areas would increase classification results. Shadowed areas were identified using a 1m DEM (Digital Elevation Model), acquisition meta data, and the ArcGIS tool 'Area Solar Radiation'. We masked all the shadowed areas, and excluded the potential planting points that fell in these areas. However, we did not manage to increase the classification results. It does not seem that shadowed areas affect the results, especially since only 4% of the total number of potential planting points fall under shadowed areas.

3.1.4. Conclusion

Spectral unmixing has some potential for identifying the dominant materials of pixels. Looking more closely at certain unmixing images, it is clear that a distinction of certain material was made. Indeed, figure 18, the concrete sidewalks are apparent and much brighter than any surrounding area. Visually, it would appear that the unmixing algorithm did indeed manage to separate concrete. Perhaps, the decision tree classification was not best suited for the final classification. Also, the lack of atmospheric corrections may have created some confusion during classification. Figure 19 shows imagery of the same scene on two different acquisition dates. The illumination is different and depends partially on atmospheric conditions. The low success rates of the classification presented in these preliminary studies lead us to pursue a new methodology.



Figure 18 Concrete represented as bright pixels after linear spectral unmixing showing the potential for identifying urban surface materials



Image taken on 23/08/2016: Sun at 56° over the horizon and looking almost completely South



Image taken on 2/09/2016: Sun at 45° over the horizon and looking South-East

Figure 19 Differences in illuminations of two CASI images of the same scene taken on two separate days with different atmospheric conditions

Images with a metric resolution provide a general understanding of urban surface materials and can be used as a preliminary dataset to assess the costs and optimal locations of planting. Figure 20 is an example of the type of cartography achieved with this method. Due to the large confusion between asphalt and concrete we grouped these two classes into one category named inert materials. Also, since this particular scene was taken with an overlap of two flight lines, any point in these overlap that did not have the same classification on both occasions was reclassified as ‘unknown materials’. For example, if a point on one flight line was classified as vegetation, but the same point on a different flight line was classified as asphalt, then it was deemed ‘unknown material’.



Figure 20 Urban surface materials at potential planting points of a portion of Montreal North, Montreal, (QC) Canada

3.2. Multispectral imagery RGBI

3.2.1. K-means algorithm

The tests performed with the RGBI (Red, Green, Blue, Infrared) imagery were only performed on one tile (#0011). This tile covers an area of approximately 1.6km x 1.6km with a 20cm ground resolution. The tile was classified with a K-means algorithm. This algorithm is an unsupervised classification that separates the spectral space along n-axes in our case: red, green, blue, and infrared. The number of clusters (K) is defined by the user and will represent the number of classes at the output. The algorithm uses the digital numbers of a sample set of pixels (also user defined). By iterative process, the algorithm finds the centre of gravity of the K clusters. Then each pixel is classified into a cluster in a way that minimizes the spectral distance E between the centre of gravity of the cluster and the pixel value (equation 7) (PCI Geomatics 2017). The results are the K-clusters that need to be assigned to a specific class.

$$E = \sum_{i=1}^k \sum_{x \in C_i} |x - m_i|^2 \quad (7.)$$

In this equation, x is a spectral representation in space of the object, m_i is the mean of cluster C_i .

For the purpose of this test we limited the processing to the public areas of the tile. This reduced the overall computation requirements of the algorithm.

3.2.2. Results and validation

We ran the algorithm to produce 16 groups of pixels. These groups were reclassified into 7 classes by photo-interpretation as follows: 0- unknown, 1- shadows, 2- trees and high vegetation, 3- low vegetation, 4- asphalt, 5- concrete, and 6 – very bright objects. Figure 21 shows the results of the classification after photo-interpretation over a portion of the Montreal North.



Figure 21 Urban surface materials of a portion of Montreal North using K-means clustering with RGBI 20cm ortho-images

With unsupervised classifications, it is hard to match final classes with a predefined set of classes. This is the case in our study, the K-means clusters output does not match the desired materials we want to identify provided by the City. Therefore, we were unable to use the geo-located points for validation purposes. Instead, we validated the K-means classification by photo-interpreting points into the same categories of the final output. With a sample of 257 points we managed to obtain an 82% success rate. Since the proportions of the classes were not equal, we had to normalize the number of validation points per class. This normalization actually increases the overall success rate to 87%.

Similarly, to the CASI images, we eliminated validation points that fell in shadow areas to see if we could increase the success rate. However, due to the difficulty of masking shadowed areas, we only had 40 points to test the overall success rate of the K-means classification without shadow. We obtained 83% success rate, which increased to 96% when we normalized by class.

To validate the classification, we created confusion matrices that provided us with overall success rate. From these we calculated the Kappa coefficient, and the variance of the kappa coefficient. We performed a z-score test to ascertain the difference between the classifications with and without points in shadows (see chapter 5 for further explanations for validation procedures). Table 1 recapitulates the results of the two classifications. Table 2 shows the z-score of the pairwise comparison

Table 1 Kappa coefficient and Variance of kappa coefficient of K-means classification with RGBI images

Classifications	Kappa	Variance
K-means VS photo-interpretation	0.758	0.556
K-means VS photo-interpretation with points in shadowed areas	0.610	0.614

Table 2 Significance test using Z-score between K-means classification of RGBI images with points under shadows and without points under shadows (NS- not significant)

Pairwise comparison	Z	90%	95%	99%
Photo-interpretation with points under shadow VS without points under shadow	0.179	NS	NS	NS

Degree of confidence	90%	95%	99%
Z-score (left tail)	-1.645	-1.95	-2.575
Z-score (right tail)	1.65	1.95	2.575

3.2.3. Conclusion RGBI images

The K-means results are very promising. The RGBI images with a sub-metric resolution seem to produce an accurate identification of surface materials. Fewer pixels are mixed and it is easier to delimit objects in the images. They produce better results than the CASI images. However, the RGBI tests were limited to one tile which does not allow us to ascertain the feasibility of the K-means methodology with more data. We would need to try the methodology with more tiles before pronouncing one method better than the other. Also, the K-means algorithm is hard to reproduce over many tiles, as the output classes are not defined. Each new K-means on each tile may produce different classes that would need to be photo-interpreted. What is more difficult would be overlapping tiles with different clusters. It seems unlikely that this methodology would allow us to identify urban surface materials over a large area.

3.3. Conclusions on preliminary results

With the images at our disposal CASI 1500 with metric spatial resolution, and RGBI ortho-images with sub-metric resolution we obtained better results using an unsupervised K-means classification on the sub-metric images. However, as discussed in section 3.2.3., it doesn't seem viable to use these images to identify urban surface materials over a large territory. However, the results with the metric images (CASI1500) were less than satisfactory. Although linear spectral unmixing seems to be one of the more common approaches for urban studies with hyperspectral images, in our case it produces low classification results. This may be due to the lack of atmospheric corrections to establish more representative spectral signatures. Visually speaking, the spectral linear unmixing seems to function well. We have therefore, decided to pursue further tests using reference spectral signatures but with a different methodology. Chapter 4 describes this new methodology.

Chapter 4 – Methodology

This chapter covers the main methodology used for identifying surface materials in the City of Montreal. We used the same CASI 1500 aerial imagery as in the preliminary studies. See chapter 3 (section 3.1.) for more detail on the acquisition of the images. We go over the specific study area, and the steps of the methodology depicted in the following flowchart (Figure 22). The first step is choosing a study site, and preprocessing the hyperspectral data. The second step involves defining a robust methodology for identifying surface materials. Then, based on the methodology chosen we calculate metrics for surface material classification. Finally, the last step assesses the validity of the classification obtained. Each step is further described in the next sections.

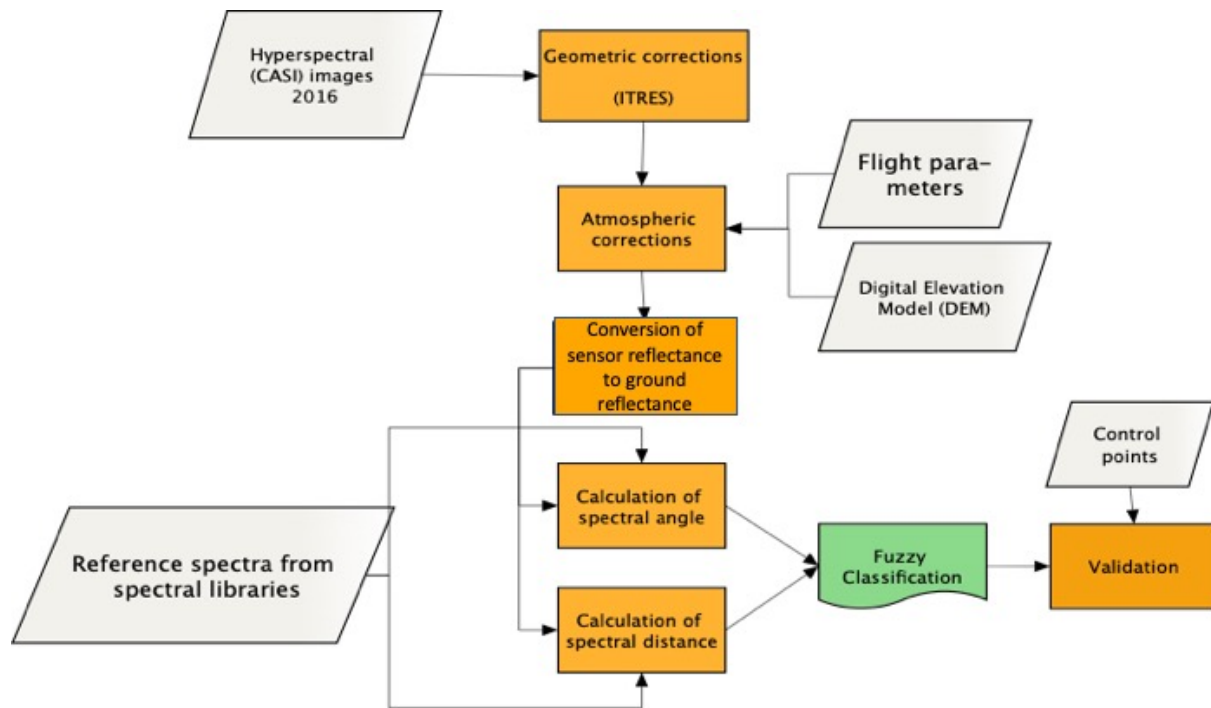


Figure 22 Flowchart of the fuzzy classification methodology used to identify urban surface materials with hyperspectral data

4.1. Study area

The study area is located on the Island of Montreal, Quebec, Canada. It is the second largest metropole within Canada, and has population of approximately 1.7 million people. It is a vibrant city that holds a large industrial zone, and many commercial and residential areas. As the largest city in the province of Quebec it attracts a lot of business, and people. Home to an ever-growing population, the city of Montreal necessitates a proper understanding and management of its structures and urban fabric to ensure a livable, and sustainable development.

Different areas of Montreal are dominated by various types of materials. Indeed, the industrial and commercial areas are primarily built with construction materials such as asphalt, cement, and tar. These areas are sparsely vegetated, or bare of vegetation. In contrast, the residential areas tend to have more trees, parks, and green spaces. However, the built parts of residential areas are still composed primarily of construction materials, mentioned previously, but often included more permeable ones such as cobblestones. Rooftops over the entire island encompass a large portion of the visible structures of aerial imagery. In Montreal, they are often made of shingles of different colours (black, red, green), sometimes, the shingles are made of slate, or wood. Moreover, as Montreal is a large metropolitan city, it has an extensive road network that is primarily built with asphalt and tar. Less built areas include a number of parks. The largest and most central one is Mount Royal located in the centre of the island. Other large parks include the botanical garden located near the Olympic stadium, Park Maisonneuve, La Fontaine Park, and many more interspersed across the island. Figure 23 is a land-use map of the Island of Montreal.

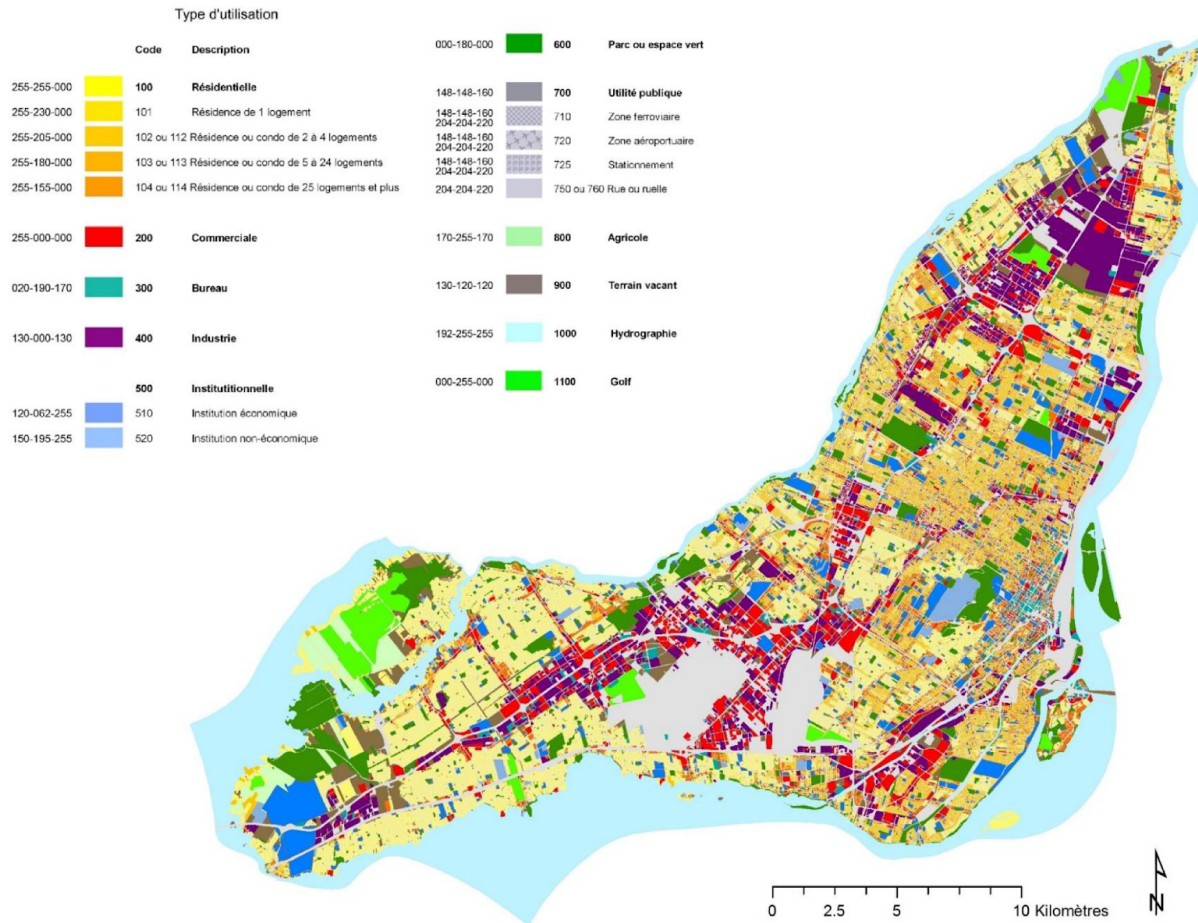


Figure 23 Map of Montreal, Qc, Canada, showing the main land uses (source: Communauté Métropolitaine de Montréal (CMM), website: <http://cmm.qc.ca/donnees-et-territoire/observatoire-grand-montreal/produits-cartographiques/cartes-pdf/>)

The tile we looked at in particular was taken on August 20th 2016, named CASI_2016_08_20_10345.h14v1 (Figure 24). It was chosen because it covered an area next to the Department of Geography of the University of Montreal. This made fieldwork (obtaining field spectral signatures) more convenient. The tile covers the main buildings of the University of Montreal, some residential areas in the boroughs of Outremont and Côte-des-Neiges. The residential areas have large houses with variable roofing materials. These neighborhoods also have large apartment buildings. Asphalt streets are flanked by concrete sidewalks. A number of large deciduous and coniferous trees separate house entrances and the residential roads. The neighborhoods also has small parks, with artificial soccer fields, grass areas, benches and waterworks.



Figure 24 Study area for fuzzy classification tile CASI_2016_08_20_103450h14v1

4.2. Methodology

This section of the methodology is divided into three steps the pre-processing of the images, finding the reference spectral signatures, and finally the processing of the images.

4.2.1. Preprocessing: Atmospheric Corrections

In our laboratory, the 6S code was modified to better suit the aerial imagery used in the project. The 6S code separates the atmosphere into 34 layers for which it considers the effects of gases and aerosols on solar radiation. On one hand, gases can absorb and scatter solar energy depending on atmospheric profiles (pressure, temperature, water vapour content, and ozone content). On the other hand, aerosols tend to scatter photons in a given direction based on the sun's angle, and the sensor's angle. The 6S code also takes into consideration the terrain by adding altitude. In our case we assume the terrain to be more or less flat at 100m. We considered an infinite Lambertian surface as a target. We therefore, did not take into consideration environmental reflectance that can distort target reflectance (Equation 2). We will now look at two models that describe the atmospheric interactions and the aerosol interactions of solar irradiance.

4.2.1.1. Gaseous transmittance

For each layer, we need to know the vertical profiles of pressure and temperature to calculate the absorption and scattering on both the downward and upward paths (Bouroubi et al. 2018). The gas absorption depends on the concentration of the various gases in the atmosphere (oxygen, nitrogen, methane, carbon dioxide, etc.). These gas concentrations are supposed constant except for water vapour and ozone. In our case the default profiles given by the standard model mid-latitude summer were adjusted. Total ozone was adjusted with values taken from climatology data, while water vapour content was adjusted from meteorological data. This was to better represent the local profiles on the date and at the time of image acquisition. In particular, total water vapour content was calculated based on the Leckner equation (8).

$$\omega = 0.493H_r P_s / T_a \quad (8.)$$

For which ω is the total water vapour content. H_r is the relative humidity, P_s is the partial pressure of water vapour in saturated air taken from meteorological records at Pierre-Elliott Trudeau Airport. P_s can be calculated with the following empirical equation (9)

$$P_s = \exp \left(26.23 - \frac{5816}{T_a} \right) \quad (9.)$$

Then we calculated the gaseous transmittance per spectral band by considering the spectral sensitivity and the gaseous transmittance per wavelength. Concerning the spectral sensitivity, we simulated the Gaussian spectral sensitivity curve with a given central wavelength and a known FWHM (full width half maximum) value (the wavelength at which 50% of the quantum efficiency of the sensor is reached). From this we estimated one standard deviation of the curve (or 68% quantum efficiency), and then calculated up to 3 standard deviation to obtained almost 99% of the quantum efficiency. This allowed us to find the average gaseous transmittance in our wavelengths. In equation 2 this would be P_R .

4.2.1.2. Scattering

Scattering due to gases can be described by Rayleigh scattering. It depends on pressure, temperature, and optical depth. It has to be calculated in each layer from the sun to the earth's surface and the return path, as this phenomenon will attenuate the energy as it moves down towards the Earth's surface. Optical depth was calculated by 6SV for 20 wavelengths and then interpolated for all other wavelengths.

Concerning the particulate scattering, there are four large categories of aerosols in the atmosphere that can cause Mie-scattering: dust, water-solubles, soot, and ocean spray. Their proportion depends on location and source of aerosols and are described in a number of models such as continental, urban, etc. We have used the urban model as we are studying the second largest metropolitan area of Canada. Mie-scattering depends on the angle of the sun and the angle of view of the sensor (see equation 2). The angle of the sun θ_s was calculated by converting the MTM coordinate of the centre of each pixel into latitude and longitude, and by knowing the time and date of acquisition. The azimuthal angle of the sensor θ_v was calculated for each direction of the

flight line (north and south) for both left and right portions of the image (Figure 25). Pre-determined viewing angles were calculated, these were at 5° , 10° , 15° , 20° , 25° , and 30° for the right and left side of the flight direction. Depending on the flight direction (north or south), the angle of view with respect to the sun would be different making the Mie-scattering potentially different (Figure 26).

For the estimation of the aerosol optical depth, we used the visibility measures of the Pierre-Elliott-Trudeau airport at the time of the image acquisition and the special computer routine from 6SV. The optical depth is estimated at 550nm. This value is used to estimate the optical depth at 20 different wavelengths (the same ones as for the Rayleigh scattering) using the properties of the chosen aerosol model.

Using the Rayleigh and Mie-scattering parameters, it is possible to calculate all the atmospheric reflectance, as well as the scattering transmission, and the spherical albedo (Equation 2).

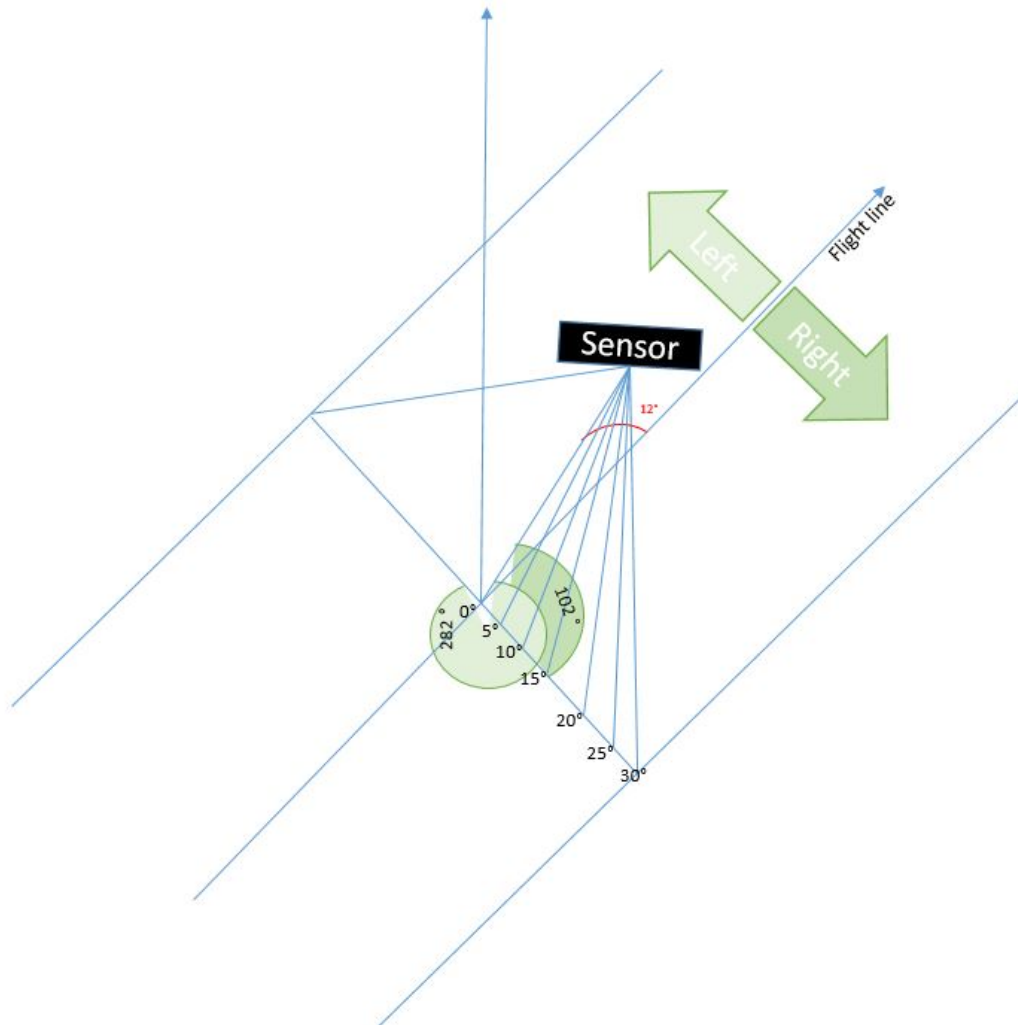


Figure 25 Schema of flight line and field of view angle in the particular case of CASI 1500 hyperspectral imagery taken over the Island of Montreal (QC), Canada

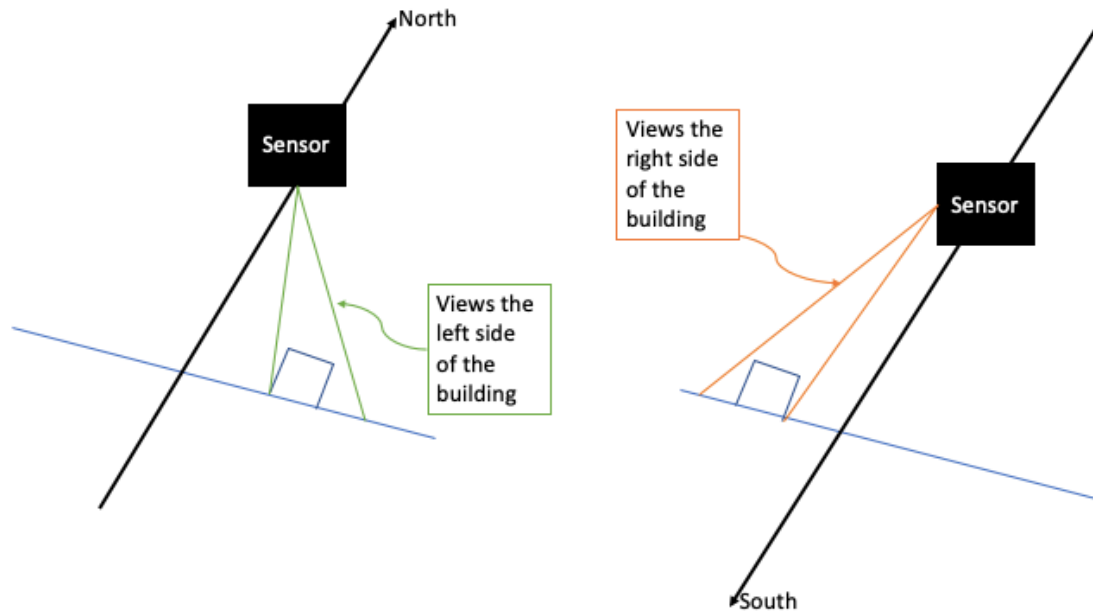


Figure 26 Field of view from aerial imagery with CASI 1500 sensor in a Northward direction and a Southward direction

After having performed these atmospheric corrections adapted to the specific conditions of our images, we realised that certain bands in the NIR were not properly corrected. We had to eliminate bands 80 to 85 (930nm and 958nm).

4.2.2. Image analysis: A combined classification methodology

The following section describes our classification method that uses the unique interactions between surface materials and solar radiation. We compared pixel spectral signatures to reference spectral signatures acquired from three libraries. The methodology combines two similarity metrics by assuming a set of classes that have fuzzy boundaries. This assumption allows pixels to be classified in a non-binary fashion, which helps with the classification of mixed pixels, and transition zones.

4.2.2.1. Reference spectra

The research method's main assumption is that one can identify objects based on their interactions with the sun's radiation (i.e. their spectral signatures). We wanted to compare our pixel spectral

signatures with reference spectral signatures. We gathered spectra from three different spectral libraries that are described as follows.

4.2.2.1.1. ASTER spectral library

The first spectral library we chose to use was the well establish ASTER spectral library (Meerdink et al. 2019). Spectra from the ASTER spectral library are taken in laboratory conditions and span a large range of both manmade and natural materials over a wide range of the EM spectrum. Three laboratories helped create the library as we know it today: The Jet Propulsion laboratory (JPL), the John Hopkins University (JHU), and the United States Geological Survey (USGS). There are over 2000 different spectra available for identification. However, using all of them would require a large computational effort. We only selected some of the spectra (Figure 27) that we thought were most likely to appear in Montreal. These included most of the manmade objects taken from the JPL library, as well as some of the vegetation spectra available from the JHU library. Figure 28 presents a few examples of spectral signatures over the a wavelength interval we were interested in, for three main categories that we used: asphalt, concrete, and vegetation.

- 1 [8U] Asphaltic_concrete_0425uuu.bt :
- 2 [8U] Asphalt_roofing_shingle_0597uuu.bt :
- 3 [8U] Asphalt_shingles_0490uuu.bt :
- 4 [8U] Black_tar_paper_0522uuu.bt :
- 5 [8U] Black_tar_paper_0523uuu.bt :
- 6 [8U] conifers.bt :
- 7 [8U] Construction_asphalt_0095uuu.bt :
- 8 [8U] Construction_asphalt_0096uuu.bt :
- 9 [8U] Construction_asphalt_0674uuu.bt :
- 10 [8U] Construction_Concrete_0092uuu.bt :
- 11 [8U] Construction_concrete_0397uuu.bt :
- 12 [8U] Construction_concrete_0424uuu.bt :
- 13 [8U] Construction_concrete_0432uuu.bt :
- 14 [8U] Construction_concrete_0598uuu.bt :
- 15 [8U] Construction_tar_0099uuu.bt :
- 16 [8U] Construction_tar_0100uuu.bt :
- 17 [8U] decidous.bt :
- 18 [8U] drygrass.bt :
- 19 [8U] grass.bt :
- 20 [8U] Reddish_asphalt_roofing_shingle_0672uuu.bt :
- 21 [8U] Reddish_asphalt_shingle_0683uuu.bt :

Figure 27 List of spectral signatures from ASTER library used as reference spectra

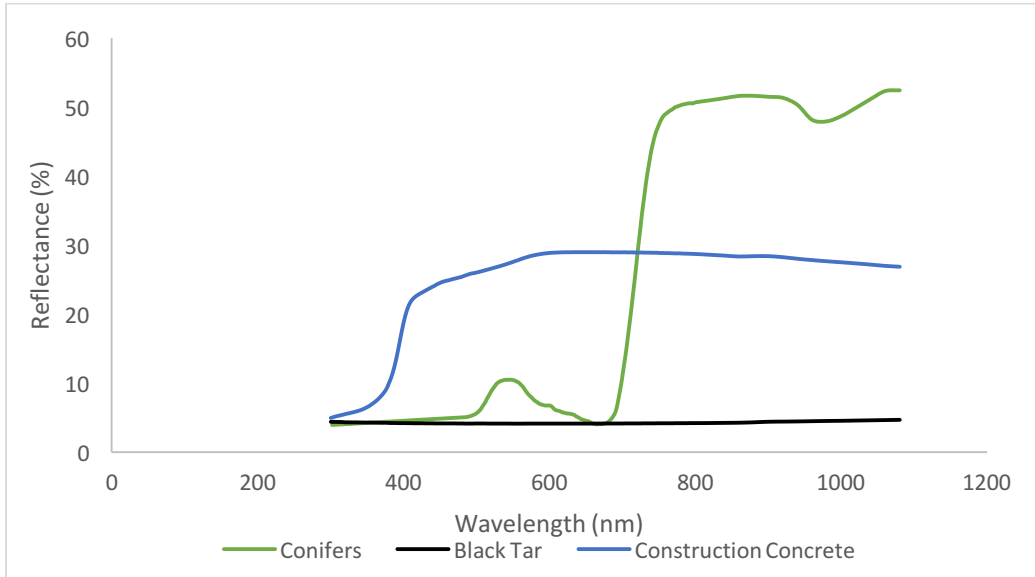


Figure 28 Graphical representation of spectral signatures in the ASTER library (conifers in green, construction concrete in blue, and black tar in black)

4.2.2.1.2. HYPERCUBE spectral library

The second spectral library we used was obtained from HYPERCUBE. Originally built as a software for analyzing imagery for military reconnoitering and operations, HyperCube is now available for other purposes and has an inbuilt spectral library. Although it is not as large a library as that of ASTER, it is more focused on urban materials. Figure 29 shows a list of the spectral signatures used in our classification. There is little information available to the public regarding the methodology used to obtain the spectral signatures. However, what we do know is that the spectral signatures were taken in the mid 90's with a photo-spectrometer mounted on a "cherry-picker" boom located on a vehicle. Real world samples were taken with the device. None of the spectral signatures were taken in laboratory conditions (as opposed to the ASTER spectral library). Delma Delbosque of the US Army Engineer Research and Development Center – Geospatial Research Laboratory, personal communication (2019), provided this information. Figure 30 shows a few examples of spectral signatures available in the HYPERCUBE library.



















-  1 [8U] Asphalt light.txt
-  2 [8U] Asphalt roofing.txt
-  3 [8U] Asphalt.txt
-  4 [8U] Asphaltdark.txt
-  5 [8U] Concrete.txt
-  6 [8U] Grass 1.txt
-  7 [8U] Grass 2.txt
-  8 [8U] Grass 3.txt
-  9 [8U] Grass, mowed.txt
-  10 [8U] Grass, sparse.txt
-  11 [8U] Pavement.txt
-  12 [8U] Road 2.txt
-  13 [8U] Trees 1.txt
-  14 [8U] Trees 2.txt
-  15 [8U] Trees 3.txt
-  16 [8U] Vegetation 1.txt
-  17 [8U] Vegetation 2.txt
-  18 [8U] Vegetation 3.txt

Figure 29 List of the spectral signatures from HYPERCUBE library used as reference spectra in the fuzzy classification

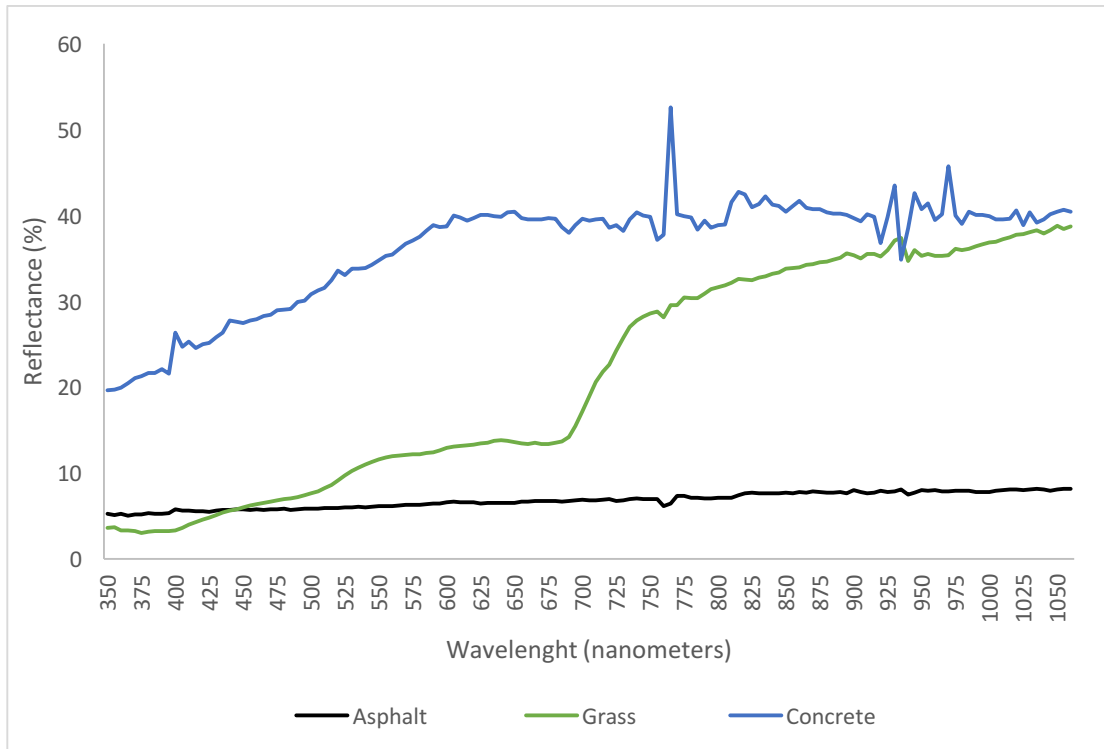


Figure 30 Graphical representation of spectral signatures in the HYPERCUBE library (grass in green, concrete in blue, and asphalt in black)

4.2.2.1.3. Spectroradiometer library

The last spectral library we chose to use was one created by us. It was based on field measures using a hand held spectroradiometer (ASD HH2). The measures were taken over two days in the summer of 2018 one on the 15th of June, the other on the 19th of June. The weather on both those days were similar (sun with a few clouds), as were the temperatures (high of 25°C on the 15th of June, and 28°C on the 19th of June). Measures were only taken when full sun was available. Spectra were taken in the borough of Outremont, near the department of Geography of the University of Montreal. The materials of interest were asphalt, cement, grass, and earth. As each of these materials can appear quite different based on age, use, and location, we chose to further separate the manmade materials in three classes: new, moderate, and old. Figure 31 provides some graphical representations of the spectral signatures obtained in the field.

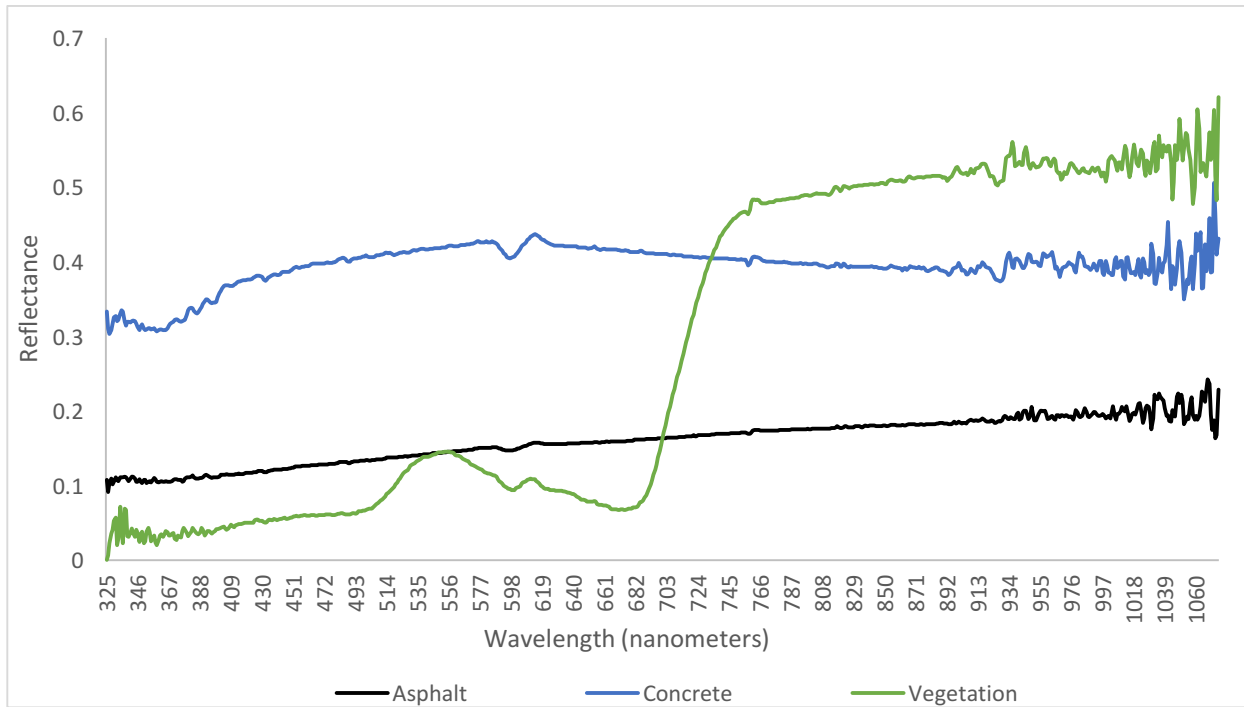


Figure 31 Graphical representation of spectral signatures in the ASD library (vegetation in green, concrete in blue, and asphalt in black)

Five samples spectra were taken for each type of material reaching a total of 40 samples. Calibrations of the spectroradiometer were performed as per manual instruction. The reference target was a circular white plate. A 25 ° field of view was used. The spectroradiometer was held perpendicular to the target by an operator about 1m above the ground when measures were taken. The measures were recorded directly in reflectance values. For each point of measure, a GPS location was also taken using a Garmin 84. Once back in the laboratory we noticed that some of the spectral signatures obtained in the field had negative values, which lead us to believe there was an error during calibration, or that the reference target wasn't taken often enough. We decided to eliminate all spectral signatures with any negative values, including all the spectral signatures representing earth, leaving us with 31 spectral signatures. Figure 32 shows the final list of spectral signatures obtained in the field with the hand held ASD.

- 1 [8U] AsphalteM_00025_gps026.txt
- 2 [8U] AsphalteM_00030_gps031.txt
- 3 [8U] AsphalteM_00033_gps034.txt
- 4 [8U] AsphalteN_00009_gps010.txt
- 5 [8U] AsphalteN_00012_gps013.txt
- 6 [8U] AsphalteN_00014_gps015.txt
- 7 [8U] AsphalteN_00015_gps016.txt
- 8 [8U] AsphalteV_00023_gps024.txt
- 9 [8U] AsphalteV_00037_gps038.txt
- 10 [8U] AsphalteV_00038_gps039.txt
- 11 [8U] AsphaltN_00004_gps005.txt
- 12 [8U] AsphaltV00008_gps009.txt
- 13 [8U] BetonM_00000_gps001.txt
- 14 [8U] BetonM_00001_gps002.txt
- 15 [8U] BetonM_00002_gps003.txt
- 16 [8U] BetonM_00007_gps008.txt
- 17 [8U] BetonM_00011_gps012.txt
- 18 [8U] BetonN_00003_gps004.txt
- 19 [8U] BetonN_00010_gps011.txt
- 20 [8U] BetonN_00017_gps018.txt
- 21 [8U] BetonN_00018_gps019.txt
- 22 [8U] BetonN_00020_gps021.txt
- 23 [8U] BetonV_00005_gps006.txt
- 24 [8U] BetonV_00006_gps007.txt
- 25 [8U] BetonV_00013_gps014.txt
- 26 [8U] BetonV_00019_gps020.txt
- 27 [8U] BetonV_00022_gps023.txt
- 28 [8U] GazonVertJaune_00027_gps028.txt
- 29 [8U] GazonVert_00016_gps017.txt
- 30 [8U] GazonVert_00021_gps022.txt
- 31 [8U] GazonVert_00024_gps025.txt

Figure 32 List of spectral signatures from ASD library

4.3. Image Processing

Image processing involved a multi-step method as seen in the flowchart (Figure 22). The first step is calculating the similarity metric using a spectral angle. The second step was to determine reflectance differences between reference spectral and pixel spectra by calculating the total distance between the two curves. And finally, we combined these two metrics in a fuzzy classification.

4.3.1. Similarity metric: Shape

The first step of the analysis involved comparing the shapes of pixel spectra to reference spectra and estimating the degree of similarity between them. In order to accomplish this, we were inspired by a common hyperspectral classification method mentioned in Chapter 2, the spectral angle mapper or SAM. This classifier calculates the angle in n -dimensions between a reference spectral signature and a pixel spectral signature. The smaller the angle between the two spectra, the more likely they resemble each other. A user defined threshold determines the acceptability of the calculated angle and classifies the pixel to its closest resembling reference spectra. If no spectra resemble the pixel's spectral signature then it is classified as unknown.

Instead of creating a user defined threshold to classify each pixel, we simply used the calculate angle to estimate the resemblance in shape. Equation 3 (Chapter 2), describes the angle calculations in radiance which we decided to convert into degrees. It can take values between 0° and 90° . It is modified from its original form by calculating the sine instead of the cosine angle between the two spectral signatures. In this way, the more similar the shapes are, the higher the spectral angle. Figure 33 gives an example of the results of only processing for shape similarity. It compared the pixels in the image to a grass reference spectral signature taken from the ASD spectral library. The lighter shades of grey indicate a higher likeliness that the pixel spectral signature has the same shape as the reference spectral signature for grass.



Figure 33 Example of output image after running the shape similarity metric testing for a reference spectral signature representing grass from ASD spectral library (light shades of grey indicate pixels that are more likely to resemble grass, while darker shades are less likely to resemble grass)

4.3.2. Similarity metric: Distances

As we have mentioned previously, comparing the shapes of the image pixel spectral signature to reference spectra is not enough to obtain a complete and accurate classification, as many spectral signatures resemble each other. Indeed, asphalt and cement have two similar spectral signatures in their shape, but the reflectance values are different (Figure 12, Chapter 3). That is why we decided to calculate the distance between the pixel spectral signature and the reference spectral signature following a simple Euclidean distance formula in n -dimensions of the images. Equation 10 describes the calculation for this step, where V_{image} is the image spectra n dimensions, and V_{spectra} is

the reference spectral vector n dimensions. The results obtained are multiplied by 10, so that the distance similarity metric has values between 0 and 100.

$$dis = \sum (Vimage(n) - Vspectre(n))^2 \quad (10)$$

4.3.3. Fuzzy Classification

In order to combine both of the similarity criterion we decided to perform a fuzzy classification. Fuzzy classification is an interesting framework to use as it allows overlap between class borders which can help determine the classification of pixels that are in transition zones, or of materials that are inherently mixed.

Fuzzy classification is a classification that has unclear boundaries between its classes. It is based on fuzzy mathematics. Indeed, in classical mathematics objects in a given space can be classified in classes (also known as sets). These sets have crisp boundaries. That is to say each set's components are unique and only belong to a given set. That is why these boundaries are described as crisp boundaries. However, in fuzzy classification, sets have fuzzy boundaries, as the name would indicate. Fuzzy sets have three zones that describe how components interact with a given set. The first one is the zone in which a component clearly does not belong to the set by being out of the fuzzy boundary area. The second, is the inverse in which a component clearly belongs to the given set by being in a zone within the boundaries. The third zone is the fuzzy boundary area in which, components are not clearly and unmistakably part of a set. Figure 34 describes simply these three zones: where a clearly belongs to set A, b clearly does not belong to set A, and where c may belong to set A (Ross 2010).

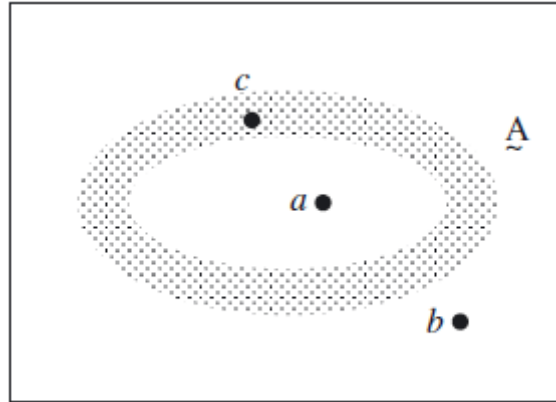


Figure 34 Description of the three possible zones in a fuzzy set A , where a is in the set, b is outside the boundaries of the set, and c is in the fuzzy boundary of the set (source: Ross 2010)

In this case, set A has fuzzy boundaries and each component can be described by its membership function to set A . Indeed, when a component belongs completely to a given set, then its membership to the set has a value of 1. This is the case of component a . Contrariwise, when a component does not belong at all to a set, then its membership to that set has a value of 0. This is the case of component b . Finally, component c has a membership to set A between 0-1. As component c is relatively closer to the inside of the set boundaries, the component will have a value closer to 1. All components of a set are described by a membership function that can be graphed. This curve has three zones: the core of a membership function, the support of a membership function, and the boundaries of a membership function. The core describes the area where objects or components belong to a set, the support describes the area where membership values are greater than 0, and finally the boundary describes the zone where membership values are greater than 0 but less than 1 (Ross 2010). Figure 35 graphically explains the three zones in which $\mu(x)$ is the membership function for a given x .

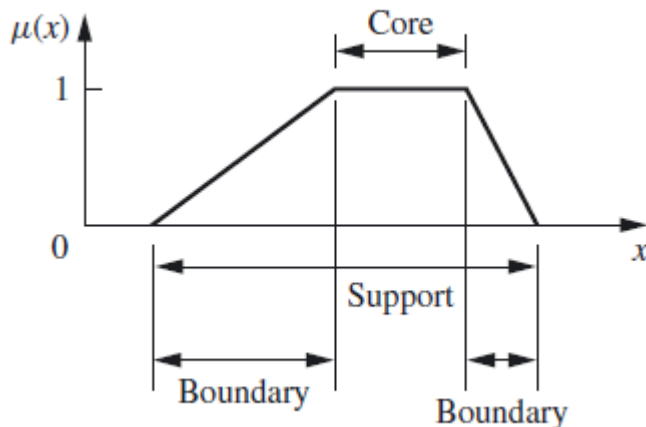


Figure 35 Membership values ($\mu(x)$) based on the boundaries of a set belonging to a fuzzy classification (source: Ross 2010)

Membership function can take many shapes, and describe the classification of different types of objects in varying types of classes. For examples, a triangular shaped membership function represents the margin of error when taking a measure with a tool (e.g. ruler). However, a trapezoidal membership function can describe descriptive classes such as the perception of height into three classes: ‘Short’, ‘Average’, and ‘Tall’. Many membership function shapes exist, the previously mentioned ones are two common examples. To obtain the membership function of overall height taking into consideration both the measure and the perception, one can combine these two shapes (triangular and trapezoidal) and obtain a completely new membership function (Ross 2010).

So far, in fuzzy classification, the fuzzification process has been described, which has explained how data can belong at different rates to given classes. However, in image classification, the output of any classification should be a clear-cut class. In order to do this, one must perform a defuzzification and eliminate the ambiguity of membership to a class. Many methods exist to defuzzify a fuzzy interpretation of data. Here are described some of the more common ones. Taking the maximum membership function entails taking the class to which the membership values is maximized. Another common method is the centroid method, that takes the defuzzification values where the curve’s centre of gravity can be found. Finally, the weighted average method, weighs each membership function by its maximum membership value. Defuzzification gives a final crisp classification of ambiguous data (Ross 2010).

For each criteria (shape and distance), three classes were created describing the similarity between reference spectra and pixel spectral. These three classes of similarity were: “Low”, “Medium”, and “High”. As is often the case in fuzzy classifications, the classes take a trapezoid form with the following limits for both criteria: {0, 20, 50} for the low class, {25, 50, 75, 80} for the medium class, and {75, 80, 90, 100} for the high class, except for the distance high class which has the following limits {75, 80, 100}. Figure 36 schematizes the fuzzification set up. Each pixel is compared to all reference spectra, and the combination receive a score both for the shape (angle), and the distance.

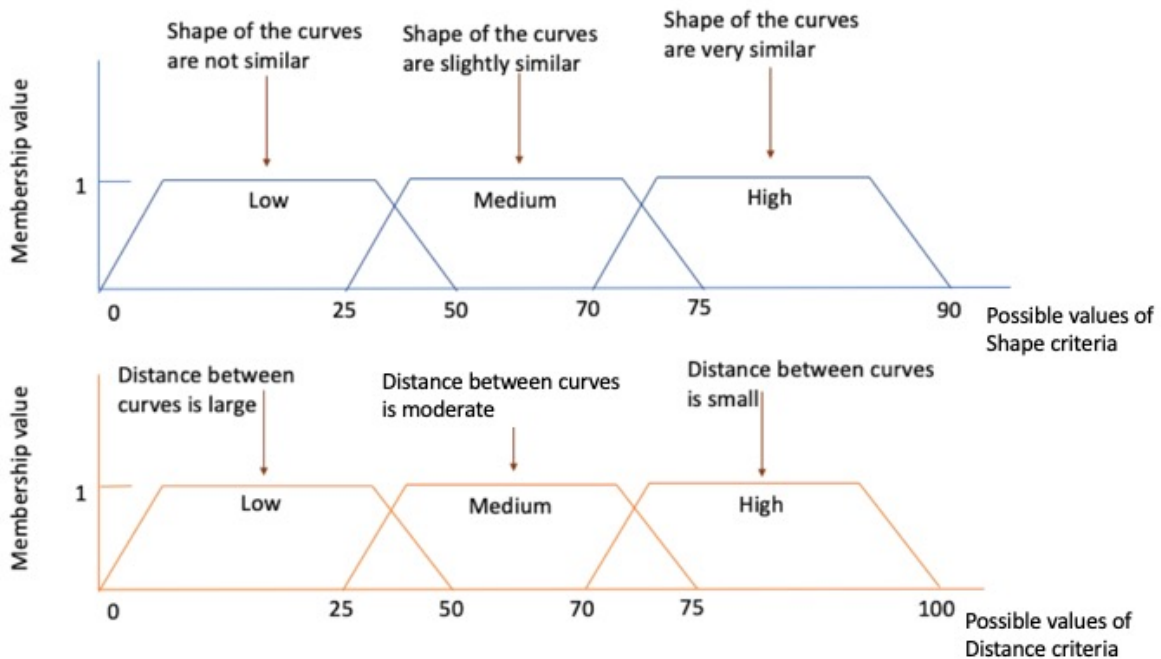


Figure 36 Schema of the fuzzy classification with set boundaries for the shape and the distance criteria

The combined results of the membership of shape and distance are created by simply combining the portions of the relevant trapezes. Figure 37 is trying to illustrate the combined weight of the two criteria that are taken into consideration. In this state, the classification is still fuzzy. A defuzzification step has to occur in order to obtain the final classification. We chose to use the maximum value of the new set (which is the combination of both criterion). Defuzzified values range between 0 and 100, with 0 being a very low likelihood of and 100 being a very high likelihood.

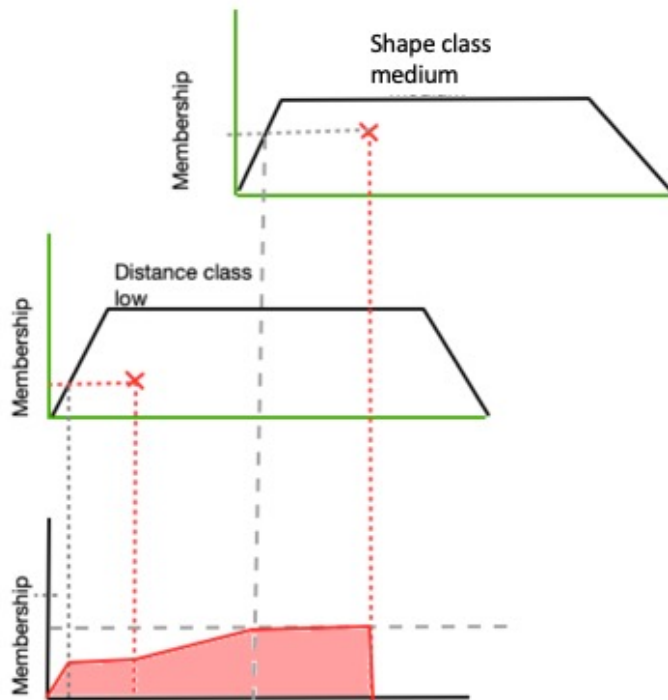


Figure 37 Schema representing the combination of both shape and distance criterion for the fuzzy classification

The final output is an image with as many bands as reference spectra tested. At each band, every pixel in the image was analyzed with the previously mentioned method that gave them a score between 0 and 100 giving the likelihood they match the reference spectra. The final classification was performed using the EASI Modelling module in PCI Geomatica (2017). The object of this classification was to extract from each pixel the band that had the maximum value to determine the best matching spectra.

Chapter 5 – Results and Discussion

This chapter explores the results obtained with the fuzzy classification described in the previous chapter. We present validation tests calculated for each classification separated by reference spectral library. To validate this methodology, we generated 50 points within the study area and proceeded to a photo-interpretation of these points. We chose to generate 50 points because we estimated it was a proper sample size to reach 95% confidence in our results. The points were distributed amongst 3 classes: asphalt, concrete, and vegetation. As the study area was primarily composed of asphalt, we assigned 26 pixels to belong to that class, while vegetation received 14 points being the second largest land cover, and concrete had a total of 10 points as it was the smallest land cover of the scene. The points were created in a vector format so that we could extract the final results of the classification with the VSAMPLE tool in PCI Geomatica (2017), for each reference library. We then determined if the class of the library matched the photo-interpretation.

We created confusion matrices for each classification and calculated the kappa coefficient to assess the classification quality. We also calculated the standard deviation from which we derived the variance. These metrics were used to calculate a Z-score, to assess if using different libraries really did have a significant difference in our results.

To calculate overall accuracy of the classification, we needed to take the proportions of properly classified points from the total number of points (Equation 11). This gave us the success rate of the classification.

$$\text{Overall Accuracy} = (Aa + Bb + Cc) / \text{total number of points} \quad (11)$$

We also present a table with producer accuracy, user accuracy, omission and commission error that are inherently linked to the confusion matrices. Producer accuracy is the total number of correctly classified points in proportion to the total number of points that should be in the class. User accuracy is the total number of points classified correctly in proportion to the total number of points classified in the same class. Omission error is defined as not including a point into the

category it belongs to, while commission error is the opposite, it is defined as including a point into a class it does not belong to (Colgalton and Grenn 1999).

The success rate of the classification alone is not enough to assess the accuracy of the classification. We needed to make sure the results are not obtained by chance by performing a Kappa analysis. The KHAT test is an approximation of the Kappa. It assesses the difference between the properly classified data (overall accuracy) and the misclassified data (sum of rows and columns). The following formulas describe the Kappa analysis (Equation 12), where p is the overall accuracy and m is the chance agreement k describes the KHAT value.

$$k = (p - m)/(1 - m) \quad (12)$$

Furthermore, the standard error of the kappa analysis can be calculated with the following formula (Equation 13), and the variance can be calculated by squaring the standard error (Equation 14):

$$SE = \sqrt{\frac{1}{(1 - p)^2 N} (p^2 + p - \sum_{i=1}^i m_r m_c (m_r + m_c) / N^3)} \quad (13)$$

$$Var = SE^2 \quad (14)$$

Where m_c is the sum of the columns, m_r is the sum of the rows, N is the total number of points used for the validation.

With the variance, we can calculate the z-score to assess if there is significant difference between the kappa's of each confusion matrix.

Let the null hypothesis $H_0: (k_1 - k_2) = 0$ and $H_1: ((k_1 - k_2) \neq 0$

The Z-score calculation is as follows (Equation 15).

$$Z = \frac{|k_1 - k_2|}{\sqrt{Var_1 - Var_2}} \quad (15)$$

If the z-score is larger than $Z_{\alpha/2}$ the null hypothesis is accepted and the two confusion matrices are not significantly different. If the z-score is smaller than $Z_{\alpha/2}$, then we can accept the alternate hypothesis. For the purpose of this study we will choose $\alpha = 0.05$, allowing us to assert the significance of our results with 95% confidence (Colgalton and Grenn 1999).

5.1. Results

5.1.1. Confusion matrix for ASTER

Using the ASTER library for reference spectra produced an overall accuracy of 94% with a Kappa coefficient of 0.903 (+/- 0.054) (Table 3). For all three classes producer accuracy is very high with values equal to, or above, 90%. User accuracy is also very high for all three classes reaching 100% for vegetation but only reaching about 82% for concrete. This lower user accuracy is explained by the high omission error reaching 10%, and the high commission error reaching about 18% for the concrete class (Table 4). Overall, the ASTER library produces a good classification with our methodology.

Table 3 Confusion matrix using ASTER library as reference spectra with N=50 comparing three classes, Asphalt, Concrete, and Vegetation

SE	0.063				
Kappa	0.869	Truth			
OvAcc	0.92	Asphalt	Concrete	Vegetation	SUM
Predicted	Asphalt	24	1	1	26
	Concrete	2	9	0	11
	Vegetation	0	0	13	13
	SUM	26	10	14	50

Table 4 Producer and user accuracy, omission and commission error of classification with ASTER library

	Producer accuracy	User Accuracy	Omission error	Commission error
--	-------------------	---------------	----------------	------------------

Asphalt	0.92307692	0.92307692	0.07692308	0.07692308
Concrete	0.9	0.81818182	0.1	0.18181818
Vegetation	0.92857143	1	0.07142857	0

5.1.2. Confusion matrix for HYPERCUBE

Table 5 shows that the HYPERCUBE library produced an overall accuracy of 80% with our fuzzy classification. The Kappa coefficient is lower than with the ASTER library reaching only 0.642 (+/- 0.091). Table 6 shows that the producer accuracy is very high with this library for both asphalt and vegetation classes; however, it takes a clear dive when we look at producer accuracy for the concrete class. This is due the very large omission error (90%) in this class. This implies that nine concrete points out of the 10 concrete points were misclassified. Furthermore, user accuracy is high for all three classes, with the lowest value being for asphalt, only reaching 74%, which would also be due to the relatively high commission error for asphalt, reaching 26%. Indeed, all nine misclassified concrete points were classified as asphalt. There were clearly some problems when classifying points representing concrete.

Table 5 Confusion matrix using HYPERCUBE library with N=50 comparing three classes: Asphalt, Concrete, and Vegetation

SE	0.091				
Kappa	0.642	Truth			
OvAcc	0.80000	Asphalt	Concrete	Vegetation	
Predicted	Asphalt	25	9	0	34
	Concrete	0	1	0	1
	Vegetation	1	0	14	15
	sum	26	10	14	50

Table 6 Producer and user accuracy, and omission and commission error for the classification using HYPERCUBE library

HYPERCUBE	Producer accuracy	User Accuracy	Omission error	Commission error
-----------	-------------------	---------------	----------------	------------------

Asphalt	0.96153846	0.73529412	0.03846154	0.26470588
Concrete	0.1	1	0.9	0
Vegetation	1	0.93333333	0	0.06666667

5.1.3. Confusion matrix for ASD

The classification using ASD library was the second most successful one after the ASTER library. Overall accuracy reaches 88%, with a Kappa coefficient of 0.795 (+/- 0.077) (table 5). Table 7 shows that producer accuracy is high for two of the three classes (asphalt and vegetation). However, it is low for concrete reaching only 50% in producer accuracy. User accuracy reached 100% for the concrete class. While slightly lower for asphalt (83%), we obtained good results for vegetation, reached 93%. Omission error for the concrete class can explain the low producer accuracy. Half the points that should have been classified as concrete were omitted. They seem to have all been placed in the asphalt class, which has the highest commission error of 17% (Table 8) Similarly, to the classification using the HYPERCUBE library, there seems to have been some problems in classifying the concrete points.

Table 7 Confusion matrix using ASD library with N=50 comparing three classes: Asphalt, Concrete, and Vegetation

SE	0.077				
Kappa	0.795	Truth			
OvAcc	0.88	Asphalt	Concrete	Vegetation	
Predicted	Asphalt	25	5	0	30
	Concrete	0	5	0	5
	Vegetation	1	0	14	15
	sum	26	10	14	50

Table 8 Producer and user accuracy, and omission and commission error of classification using ASD library

ASD	Producer Accuracy	User Accuracy	Omission Error	Commission Error
Asphalt	0.961538	0.833333	0.038462	0.166667
Concrete	0.5	1	0.5	0
Vegetation	1	0.933333	0	0.066667

5.1.4. Comparison of confusions matrices

We used the z-score to determine if there was a significant difference between confusion matrices. The null hypothesis being that there is no difference in the fuzzy classification results when using different reference spectral libraries. And, the alternate hypothesis being that there is a significant difference in the fuzzy classification results when using different reference spectral libraries. We tested these hypotheses with a 95% confidence interval $\alpha = 0.05$. We can accept the null hypothesis with 95% confidence when the z-score is larger than $\alpha/2=0.025$. Table 9 shows the pairwise results of the significance test between classifications.

Table 9 proves that there is no significant difference (with a 95% confidence) between using ASTER spectral library, HYPERCUBE spectral library, or a field spectral library with a hand held ASD as reference spectral signatures for the fuzzy classification method presented in the study.

Table 9 Pairwise z-score to assess the significant difference between classification based on reference spectral signatures

Pairwise reference spectral libraries	Z-score	Conclusion
ASD-HYPERCUBE	1.28349562	H1 is rejected: the confusion matrices are not significantly different
ASD-ASTER	0.74380312	H1 is rejected: the confusion matrices are not significantly different

5.2. Discussion

The results indicate a high success rate for our fuzzy classification. Combining similarity metrics (angle and distance) for comparing reference spectra to pixel spectra in a fuzzy classification seems to produce promising results. In the following paragraphs, we will further discuss the classification results as well as the limits of this study.

5.2.1. Discrepancies in results

There are some evident differences between the classification results. ASTER spectral library had the best classification overall accuracy rate, while the handheld ASD classification ranks as second best, and HYPERCUBE classification comes in third place. The misclassification of concrete could seem to be the origin of these discrepancies. To understand these differences, we need to look at the spectral signatures available in each spectral library (Chapter 4, Figure 27, 29, and 32), and the spectral signatures that were retained for classification (Table 10). They are colour coded by the category they were assigned to (blue for concrete, green for vegetation, and red for asphalt) for ease in validation through the confusion matrices.

Table 10 Spectral signatures remaining after classification of each reference spectral library

Spectral library	Reference spectral signatures
ASTER: 2nm width along the spectrum	<ol style="list-style-type: none"> 1. Asphaltic concrete 2. Asphalt roofing shingle 3. Conifers 4. Construction asphalt 5. Construction Concrete 6. Deciduous 7. Grass
HYPERCUBE: 5nm width along the spectrum	<ol style="list-style-type: none"> 1. Asphalt light 2. Asphalt roofing 3. Asphalt dark 4. Concrete 5. Grass 1 6. Grass 3 7. Grass mowed 8. Road 2 9. Trees 2 10. Trees 3
Handheld ASD spectroradiometer: 1nm width along the spectrum	<ol style="list-style-type: none"> 1. Asphalt medium 1 2. Asphalt medium 2 3. Asphalt new 1 4. Asphalt new 2 5. Asphalt old 1 6. Concrete medium 1 7. Concrete medium 2 8. Concrete medium 3 9. Green grass 1 10. Green grass 2 11. Green grass 3

All three spectral libraries had at least one spectral signature retained during classification that represented concrete. However, only ASTER library had a spectral signature that took into consideration the mixed nature of asphaltic concrete. Indeed, when looking more closely at the results of the classification in ASTER, there were 10 points classified as resembling the most the spectral signature of asphaltic concrete. Of those 10 points, 8 points were covered by concrete while the other two were covered with asphalt. However, knowing that there were only 10 points that were photo-interpreted as concrete, eight seems to be a very large portion (80% to be exact). Furthermore, when we look at the classification using HYPERCUBE spectral library, only 1 of 50 points was deemed concrete. That point was in truth photo-interpreted as concrete, but this left a total of nine other concrete points misclassified. These nine points were misclassified primarily as ‘asphalt light’ (6 concrete points), and ‘Road’ (3 concrete points). In the same way, ASD spectral library classification of concrete points was not a lot better. Five of the 10 points were properly classified as concrete. The other five concrete points were classified in the asphalt category. More specifically, two concrete points resembled more ‘asphalt medium’ spectral signature, and, three others resembled ‘asphalt old’ spectral signatures.

In addition, when we looked at the shape of the spectral signature (Figure 38) ‘Asphaltic concrete’ compared to simple concrete spectral signatures from the two-other reference spectral libraries we noticed a clear similarity in shape between the two spectral signatures that represent pure concrete. They both tend to increase in the visible part of the spectrum, and then dip down slightly in the longer wavelengths of the spectrum. However, the ‘Asphaltic concrete’ spectral signature has an upward trajectory all along the range of wavelengths we were interested in.

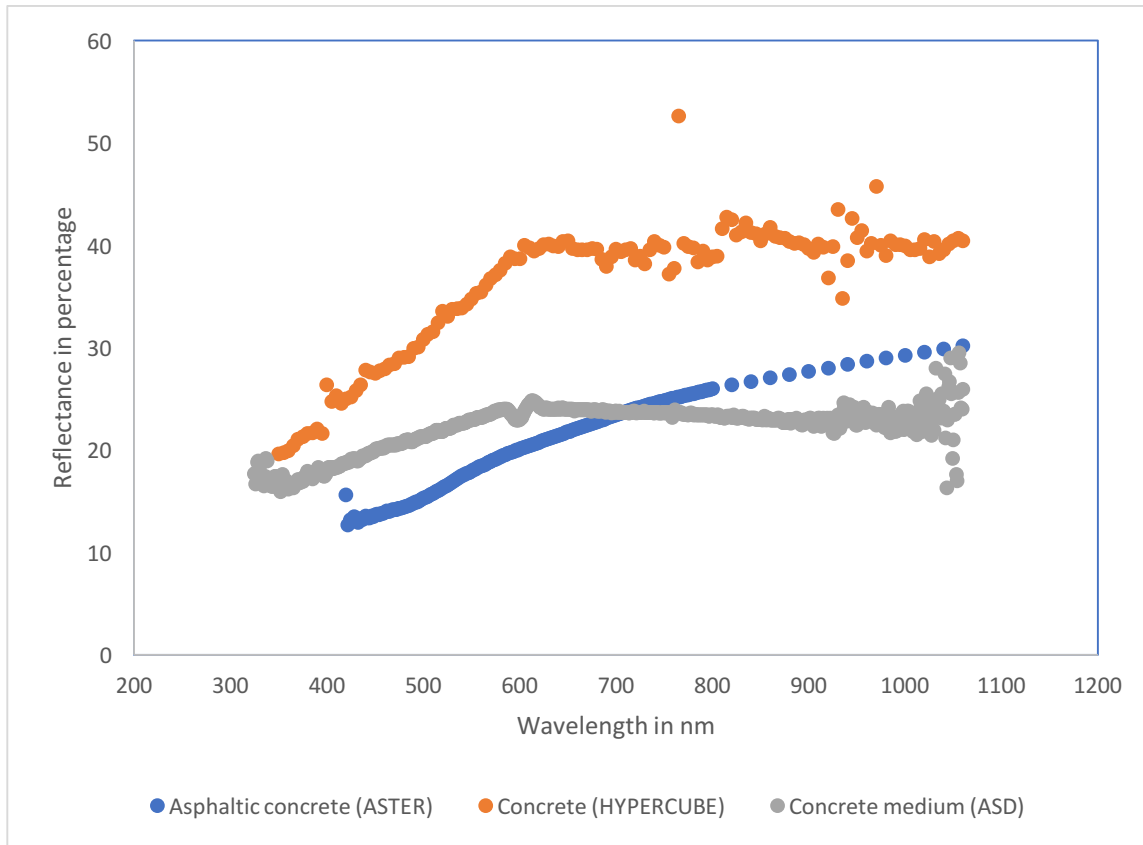


Figure 38 Comparison of spectral signatures representing Asphaltic concrete (taken from ASTER spectral library), Concrete (taken from Hypercube spectral library), and Concrete medium (taken from the handheld ASD spectroradiometer spectral library)

According to Heiden et al. (2001) a robust spectral library with references for the materials present in the image, increases success rate of identifying surface materials. We had assumed that the best results would be with the ASD spectroradiometer reference library. It would make sense that the field spectral signatures should match perfectly the image spectral signatures as the exact objects of the image were in field. However, according to our results this does not seem to be the case. The ASD spectroradiometer reference library classification was only second best, falling short of the ASTER spectral library classification. There are two possible explanations for this lower success rate: 1) poor calibration of the handheld spectroradiometer, 2) smaller diversity of input spectral signatures.

As explained in Chapter 4 (section 4.2.2.1.3.), we had to exclude some of the spectral signatures taken with the handheld spectroradiometer because of aberrant negative values. There were clearly some errors during the calibration process, either the reference target was badly taken, or the

illumination conditions changed too often, and the reference target wasn't taken often enough. It is possible that some of the spectral signatures kept for analysis were erroneous. Even though, the classification using the ASD spectroradiometer had 88% overall success rate.

As the field-spectral signatures were taken at ground level, and we did not have access to cranes or ladders, there diversity was limited. We could not access elevated materials such as rooftops or canopies. That is why only four categories of materials were taken: asphalt, concrete, grass, and earth. Even in this case, the earth category had to be completely eliminated due to poor results and its low occurrence in the study area. Asphalt spectral signatures were taken in parking lots or on roads with little to no traffic. We did not have the possibility to obtain asphalt spectral signatures on larger roads due to high volumes of car traffic during our acquisition periods. In the same fashion, concrete spectral signatures were limited to sidewalks as it was difficult to tell if certain driveways were composed solely of concrete. The most apparent lack of diversity was for the vegetation category. It was only composed of green grass. We did not make a difference between mowed or tended grass. However, the images were taken from an aerial point of view; therefore, the most common type of vegetation visible in them, would actually be deciduous and coniferous trees. These two types of spectral signatures were available in the ASTER spectral library but not in the ASD spectral library.

To continue on the idea of diverse spectral library, studies have shown that superfluous spectral signatures in the input reference spectral library can lead to poorer classification results (Bateson and Curtiss 1996). They explain that the easiest way to select endmembers (or pure pixels representing a single material) is to find endmembers within the image. In our case endmembers would then be used for the spectral signatures representing unique objects within the image. By using image endmembers, we can account for the unique environmental, and illumination conditions of the images. When using spectral libraries, with signatures taken in laboratory conditions (such as the ASTER spectral library), these specific light interactions are not accounted for. In our preliminary study (Chapter 3), we performed a linear spectral unmixing algorithm by using regions of interest directly from the images as our reference inputs. Unfortunately, the results were not promising, and barely reached 60% overall success rates. It is possible to think that the regions of interest chosen were not pure pixels. They were chosen by photo-interpretation which

has human-error. However, we explained in the preliminary results that we believe the problem was the misalignment with the validations points provided to us by the city of Montreal.

In addition, the reference spectral signatures had noise associated with them, and needed to be manipulated to coincide with the central wavelength of the CASI image bands. The noise associated with all the field measures may have caused some errors during the classifications. Field measures with the handheld spectroradiometer produced some noisy signatures in both tail ends of the spectrum (UV and near infrared) (Figure 31). In the same way, the measures taken with the spectrophotometer for HYPERCUBE produced some noise at the beginning of the spectral range (Figure 30). The reference spectral signatures from ASTER and HYPERCUBE had wavelength intervals respectively of 2 nm and 5 nm. To find the corresponding CASI image wavelength, we linearly interpolated the reflectance values based on the references. Figure 39 shows an interpolation example (over a small portion of the spectrum) for HYPERCUBE with the CASI wavelengths shown in red.

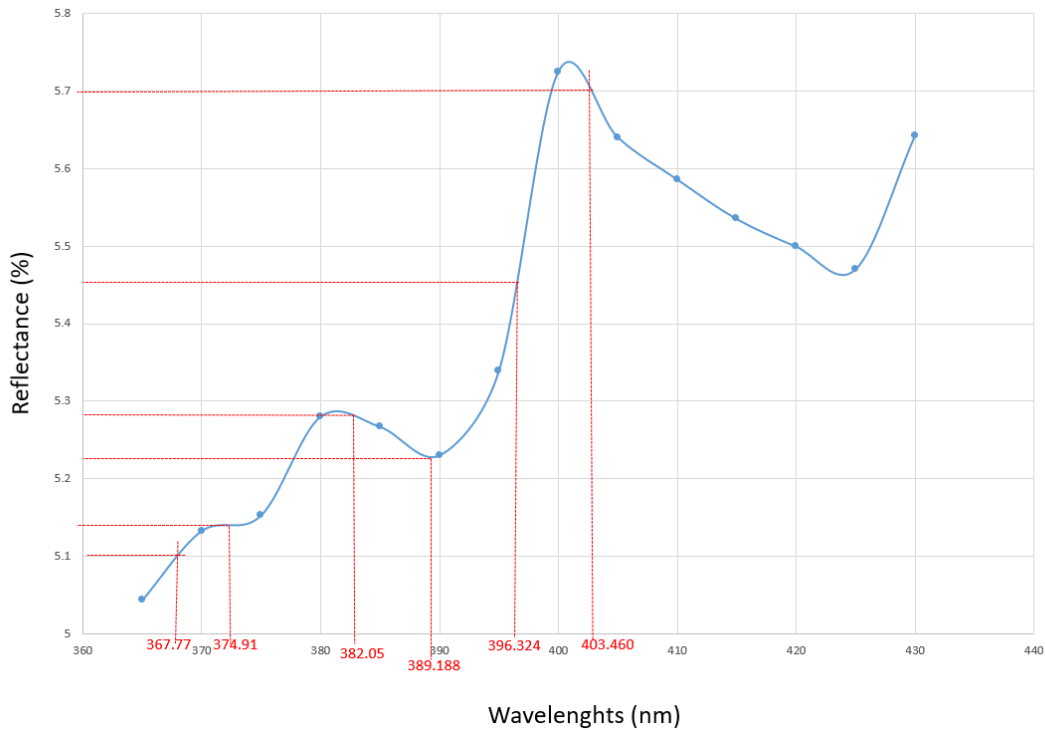


Figure 39 Interpolation of reflectance values at CASI 1500 wavelengths with HYPERCUBE spectral library

Furthermore, during the validation step of our methodology, we had a limited number of categories to test. This was in part to ease the comparison between the classifications, and in part because of the difficulty to find validation points that would account for other spectral signatures like ‘glass’, ‘copper’, and other materials. We know it was huge simplification to assume that there was only concrete, asphalt, and vegetation in the study area, but these were the most common materials in the scene.

5.2.2. Methodological errors:

A source of errors in classification could be inaccurate atmospheric corrections. They assume that our targets are infinitely Lambertian. This assumption implies that the field of view is not contaminated by adjacent target reflectance. However, in urban areas, different types of materials border targets. They can reflect energy in the sensor’s field of view and pollute the target’s radiance measure (Vermont *et al.* 1997). We also know that the atmospheric corrections did not properly correct bands 80 to 84. These five bands range between 930nm and 958nm. Eliminating these bands may have had adverse effects in differentiating similar materials. Small water vapour absorption features in the near-infrared portion of the spectrum can show key differences in spectral signatures, which is essential for identifying urban surface materials (Herold et al. 2004). It may be necessary to improve the atmospheric corrections used in the study to account for adjacency effects and near-infrared absorption feature variations.

In our methodology, we look at the similarity in reflectance values between the target pixel and reference spectra. For example, we take the sum of the Euclidian distance between the two. By taking the sum of the distances (in n-dimensions), we incur the risk of simplifying the spectral signature and rendering null the distance metric (indicating a high similarity score). Figure 40 is a graphical representation of the problem, where \vec{A} and \vec{B} are vectors of the same length with opposite directions. The sum of \vec{A} and \vec{B} would be equal to zero, making it seem that the target spectral signature is very similar to the reference spectral signature. The same pitfall is present when we calculate the spectral angle to determine the degree in similarity of spectral shapes.

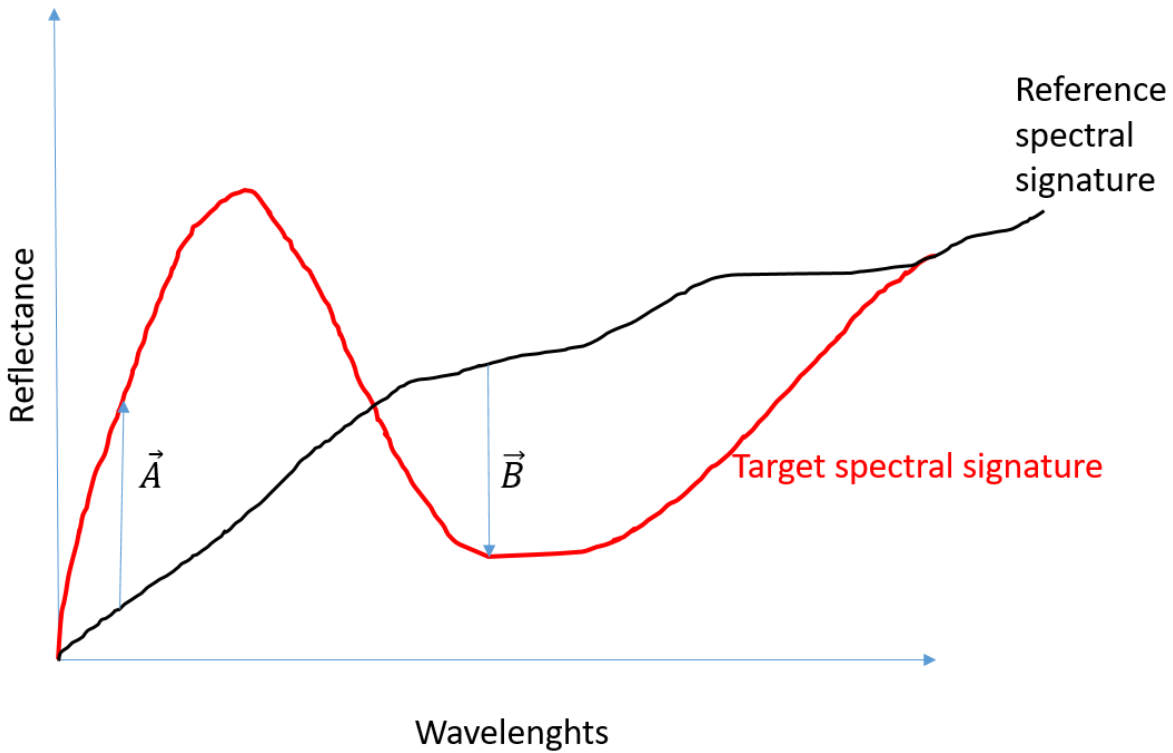


Figure 40 Distance similarity metric pitfall

5.2.3. Significant differences

One of our project's aim was to create a sound methodology to identify surface materials in urban areas using reference spectral signatures. We used three different reference spectral library to assess if the methodology would yield different results depending on the type of reference spectral signatures. We can say that the results of the three classifications are not significantly different. Meaning that the methodology works across all three types of reference spectral signatures. We assessed this significance with a 95% confidence interval.

Chapter 6 – Conclusion and future research

Two main objectives were proposed for this study. The first was to find a correspondence between the physical and chemical characteristic of objects and the spectral signatures within the images taken over Montreal, Qc, Canada. The second was to develop a sound methodology to identify surface materials in urban landscapes, with high resolution hyperspectral aerial imagery.

To accomplish these goals, we compared spectral signatures from hyperspectral images, taken with a CASI 1500 sensor, to reference spectral signatures from three different libraries (ASTER, HYPERCUBE, and an ASD field spectroradiometer). We first compared the shapes of the spectral signatures by calculating a modified version of the spectral angle. We realized that many objects in urban landscapes have similar spectral signatures. For example, asphalt and concrete have the same shape in spectral signatures, but concrete tends to have higher reflectance values. So, we decided to incorporate a score that would assess the difference in reflectance values by calculating the Euclidian distance between the reference spectral signatures and the image spectral signatures.

We combined these two similarity-metrics in a fuzzy classification that had three membership classes (low, medium, and high). The more similar the shapes and the smaller the distance between the reference spectral signatures and the pixel spectral signatures, the higher the fuzzy classification scored. To validate our results, we created confusion matrices based on 50 points that were photo-interpreted. Results are promising for all three spectral libraries. Overall accuracy was never under 80%, and reached 92% in the ASTER case.

We found that a diverse spectral library was important to increase accuracy and avoid commission and omission errors. Often, points photo-interpreted as concrete were misclassified as asphalt. We saw this particular case for both HYPERCUBE spectral library and the ASD spectral library. However, ASTER had a spectral signature that varied from concrete. It represented asphaltic concrete and seemed to help classify points deemed to be concrete.

Despite this clear error in classification, we did not find a significant difference between using any of the three spectral libraries tested. The methodology presented in this study works well for different types of reference spectral signatures. More research should be made to find a proper balance between number of spectral signatures and variation in spectral signatures of similar materials (i.e. old asphalt, new asphalt).

To further this research, I believe that adding a spatial analysis component to the study could improve the final classification. Research should concentrate on doing object based segmentation to separate materials based on texture, intensity, reflectance values, and adjacency. As urban environments are very heterogeneous it is likely to produce a large number of segments (representing different types and categories of objects). For example, separating vegetation from built materials can be accomplished with object oriented classification. Then, within these predetermined segments, we could further delimit them based on the methodology presented in this study.

Overall, this study successfully separated three types of ground surface materials (asphalt, concrete, and vegetation) using the unique interaction between ground objects and EM radiation. We also created a methodology that produces similar results across three different reference spectral libraries indicating a robust methodology. In other words, this methodology can be used by municipalities to find certain surface materials. With further research, the number of materials that can be identified will increase making this a viable alternative to field surveys.

Bibliography

- Bateson, Ann, and Brian Curtiss. 1996. 'A Method for Manual Endmember Selection and Spectral Unmixing'. *Remote Sensing of Environment* 55 (3): 229–43.
[https://doi.org/10.1016/S0034-4257\(95\)00177-8](https://doi.org/10.1016/S0034-4257(95)00177-8).
- Bonn, Ferdinand, and Rochon Guy. 1993. *Précis de télédétection : Principes et Méthodes*. 2nd ed. Vol. 1. 3 vols. Précis de Télédétection. Presses de l'Université de Québec.
- Borengasser, Marcus, William Hungate, and Russell Watkins. 2008. 'Hyperspectral Remote Sensing: Principles and Applications'. In *Remote Sensing Applications*, 130. Taylor & Francis Series. USA: CRC Press. <https://www.taylorfrancis.com/books/9780429138386>.
- Bouroubi, Yacine, Wided Batita, François Cavayas, and Nicolas Tremblay. 2018. 'Ground Reflectance Retrieval on Horizontal and Inclined Terrains Using the Software Package REFLECT'. *Remote Sensing* 10 (1638): 34.
- Breckenkamp, Jürgen, Lesley Patterson, Martina Scharlach, Wolfgang Hellmeier, and Arpana Verma. 2015. 'Definitions of Urban Areas Feasible for Examining Urban Health in the European Union'. *The European Journal of Public Health*, July, 5.
<https://doi.org/10.1093/eurpub/ckv104>.
- Burai, Péter, Balázs Deák, Orsolya Valkó, and Tamás Tomor. 2015. 'Classification of Herbaceous Vegetation Using Airborne Hyperspectral Imagery'. *Remote Sensing* 7 (2): 2046–66. <https://doi.org/10.3390/rs70202046>.
- Campbell, James B. 2007. *Introduction to Remote Sensing*. 4th ed. The Guilford Press.
- Chisense, C. 2012. 'CLASSIFICATION OF ROOF MATERIALS USING HYPERSPECTRAL DATA'. *ISPRS - International Archives of the Photogrammetry, Remote Sensing and Spatial Information Sciences XXXIX-B7* (July): 103–7.
<https://doi.org/10.5194/isprsarchives-XXXIX-B7-103-2012>.

Colgalton, Russell, and Kass Grenn. 1999. *Assessing the Accuracy of Remotely Sensed Data: Principles and Practices*. USA: Lewis Publishers.

Dobigeon, Nicolas, Jean-Yves Tournet, Cedric Richard, Jose Carlos M. Bermudez, Stephen McLaughlin, and Alfred O. Hero. 2014. 'Nonlinear Unmixing of Hyperspectral Images: Models and Algorithms'. *IEEE Signal Processing Magazine* 31 (1): 82–94. <https://doi.org/10.1109/MSP.2013.2279274>.

PCI Geomatics (version 2017-04-03). Windows. Markham, Ontario, Canada: 2017

Heiden, U., S. Roessner, K. Segl, and H. Kaufmann. 2001. 'Analysis of Spectral Signatures of Urban Surfaces for Their Identification Using Hyperspectral HyMap Data'. In, 173–77. IEEE. <https://doi.org/10.1109/DFUA.2001.985871>.

Herold, Martin, Dar A Roberts, Margaret E Gardner, and Philip E Dennison. 2004. 'Spectrometry for Urban Area Remote Sensing—Development and Analysis of a Spectral Library from 350 to 2400 Nm'. *Remote Sensing of Environment* 91 (3–4): 304–19. <https://doi.org/10.1016/j.rse.2004.02.013>.

Homayouni, Saeid, and Michel Roux. 2004. 'Hyperspectral Image Analysis for Material Mapping Using Spectral Matching'. *ISPRS Congress Proceedings*, 6.

Kadhim, Nada, Monjur Mourshed, and Michaela Bray. 2016. 'Advances in Remote Sensing Applications for Urban Sustainability'. *Euro-Mediterranean Journal for Environmental Integration* 1 (1). <https://doi.org/10.1007/s41207-016-0007-4>.

Kakhani, Nafiseh, and Mehdi Mokhtarzade. 2019. 'A New Neuro-Fuzzy-Based Classification Approach for Hyperspectral Remote Sensing Images'. *Journal of Earth System Science* 128 (2). <https://doi.org/10.1007/s12040-018-1054-9>.

Keshava, Nirmal, and John F. Mustard. 2002. 'Spectral Unmixing'. *IEEE Signal Processing Magazine*, no. 2: 44–57. <https://doi.org/1053-5888>.

- Kruse, Lefkoff, Boardman, Heidebrecht, Shapiro, Barloon, and Goetz. 1993. 'The Spectral Image Processing System (SIPS) - Interactive Visualization and Analysis of Imaging Spectrometer' *Remote Sens. Environ.* 44: 145-163. [https://doi.org/10.1016/0034-4257\(93\)90013-N](https://doi.org/10.1016/0034-4257(93)90013-N).
- Longley, Paul A. 2002. 'Geographical Information Systems: Will Developments in Urban Remote Sensing and GIS Lead to "Better" Urban Geography?' *Progress in Human Geography* 26 (2): 231–39. <https://doi.org/10.1191/0309132502ph366pr>.
- Masek, Jeffrey G. "Landsat Science." Nasa. <https://landsat.gsfc.nasa.gov> (Date accessed April 2019).
- Meerdink, Susan K., Simon J. Hook, Dar A. Roberts, and Elsa A. Abbott. 2019. 'The ECOSTRESS Spectral Library Version 1.0'. *Remote Sensing of Environment* 230 (September): 111196. <https://doi.org/10.1016/j.rse.2019.05.015>.
- Mohammadi, M. 2012. 'Road Classification and Condition Determination Using Hyperspectral Imagery'. *ISPRS - International Archives of the Photogrammetry, Remote Sensing and Spatial Information Sciences XXXIX-B7* (July): 141–46. <https://doi.org/10.5194/isprsarchives-XXXIX-B7-141-2012>.
- Moreira, R.C., and L.S. Galvão. 2010. 'Variation in Spectral Shape of Urban Materials'. *Remote Sensing Letters* 1 (3): 149–58. <https://doi.org/10.1080/01431161003692032>.
- Myeong, Soojeong, David J. Nowak, and Michael J. Duggin. 2006. 'A Temporal Analysis of Urban Forest Carbon Storage Using Remote Sensing'. *Remote Sensing of Environment* 101 (2): 277–82. <https://doi.org/10.1016/j.rse.2005.12.001>.
- Myint, Soe W., Patricia Gober, Anthony Brazel, Susanne Grossman-Clarke, and Qihao Weng. 2011. 'Per-Pixel vs. Object-Based Classification of Urban Land Cover Extraction Using

- High Spatial Resolution Imagery'. *Remote Sensing of Environment* 115 (5): 1145–61. <https://doi.org/10.1016/j.rse.2010.12.017>.
- Plaza, Javier, Antonio , Rosa Perez, and Pablo Martinez. 2007. 'Joint Linear/Nonlinear Spectral Unmixing of Hyperspectral Image Data'. In , 4037–40. IEEE. <https://doi.org/10.1109/IGARSS.2007.4423735>.
- Priya, R, and Dr M Senthil Murugan. 2013. 'Comparative Study On Hyperspectral Remote Sensing Images Classification Approaches' 4 (11): 9.
- Ross, Timothy. 2010. *Fuzzy Logic with Engineering Applications*. 3rd ed. John Wiley & Sons, Ltd.
- Segl, K., S. Roessner, U. Heiden, and H. Kaufmann. 2003. 'Fusion of Spectral and Shape Features for Identification of Urban Surface Cover Types Using Reflective and Thermal Hyperspectral Data'. *ISPRS Journal of Photogrammetry and Remote Sensing* 58 (1–2): 99–112. [https://doi.org/10.1016/S0924-2716\(03\)00020-0](https://doi.org/10.1016/S0924-2716(03)00020-0).
- Shafri, Helmi Zulhaidi Mohd, Affendi Suhaili, and Shattri Mansor. 2007. 'The Performance of Maximum Likelihood, Spectral Angle Mapper, Neural Network and Decision Tree Classifiers in Hyperspectral Image Analysis'. *Journal of Computer Science* 3 (6): 419–23. <https://doi.org/10.3844/jcssp.2007.419.423>.
- Shaw, G., and D. Manolakis. 2002. 'Signal Processing for Hyperspectral Image Exploitation'. *IEEE Signal Processing Magazine* 19 (1): 12–16. <https://doi.org/10.1109/79.974715>.
- Tyrväinen, Liisa, Stephan Pauleit, Klaus Seeland, and Sjerp de Vries. 2005. 'Benefits and Uses of Urban Forests and Trees'. In *Urban Forests and Trees*, edited by Cecil Konijnendijk, Kjell Nilsson, Thomas Randrup, and Jasper Schipperijn, 81–114. Berlin, Heidelberg: Springer Berlin Heidelberg. https://doi.org/10.1007/3-540-27684-X_5.

United Nations, Department of Economic and Social Affairs, and Population Division. 2014. *World Urbanization Prospects: The 2014 Revision: Highlights*.

Vermote, E.F., D. Tanre, J.L. Deuze, M. Herman, and J.-J. Morcette. 1997. 'Second Simulation of the Satellite Signal in the Solar Spectrum, 6S: An Overview'. *IEEE Transactions on Geoscience and Remote Sensing* 35 (3): 675–86. <https://doi.org/10.1109/36.581987>.

Waddell, Paul. 2002. 'UrbanSim: Modeling Urban Development for Land Use, Transportation, and Environmental Planning'. *Journal of the American Planning Association* 68 (3): 297–314. <https://doi.org/10.1080/01944360208976274>.

Ye, Cheng-ming, Peng Cui, Saied Pirasteh, Jonathan Li, and Yao Li. 2017. 'Experimental Approach for Identifying Building Surface Materials Based on Hyperspectral Remote Sensing Imagery'. *Journal of Zhejiang University-SCIENCE A* 18 (12): 984–90. <https://doi.org/10.1631/jzus.A1700149>.